QCD equation of state at very high temperature: Computational strategy, simulations, and data analysis

Matteo Bresciani,[1] Mattia Dalla Brida,[2,3] Leonardo Giusti,[2,3] and Michele Pepe[3]

[1]*School of Mathematics and Hamilton Mathematics Institute, Trinity College, Dublin, Ireland*
[2]*Dipartimento di Fisica, Università di Milano-Bicocca, Piazza della Scienza 3, I-20126 Milan, Italy*
[3]*INFN, Sezione di Milano-Bicocca, Piazza della Scienza 3, I-20126 Milan, Italy*

(Received 25 November 2025; accepted 22 January 2026; published 23 February 2026)

We present a detailed account of the theoretical progress and the computational strategy that led to the nonperturbative determination of the QCD equation of state at temperatures up to the electroweak scale reported in Phys. Rev. Lett. **134**, 201904 (2025). The two key ingredients that make such a calculation feasible with controlled uncertainties are (i) the definition of lines of constant physics through the running of a nonperturbatively defined finite-volume coupling across a wide range of energy scales, and (ii) the use of shifted boundary conditions which allow a direct determination of the entropy density thus without the need for a zero-temperature subtraction. Considering the case of QCD with $N_f = 3$ massless flavors in the temperature interval between 3 and 165 GeV, we describe the numerical strategy based on integrating in the bare coupling and quark mass, the perturbative improvement of lattice observables, the optimization of numerical simulations, and the continuum extrapolation. Extensive consistency checks, including finite volume and topology freezing effects, confirm the robustness of the method. The final results have a relative accuracy of about 1% or better, and the errors are dominated by the statistical fluctuations of the Monte Carlo ensembles. We also compare our nonperturbative results with predictions from standard and hard thermal loop perturbation theory showing that at the level of %-precision contributions beyond those known, including nonperturbative ones due to ultrasoft modes, are relevant up to the highest temperatures explored. The methodological framework is general and readily applicable to QCD with four and five massive quark flavors and to other thermal observables, paving the way for systematic nonperturbative studies of thermal QCD at very high temperatures.

DOI: 10.1103/jl9n-lk9k

I. INTRODUCTION

The study of the thermodynamics of QCD is central to our understanding of strongly interacting matter under extreme conditions, with direct implications for cosmology [1,2] and heavy-ion physics [3,4]. A key challenge is the reliable determination of equilibrium properties from first principles across energy scales where perturbation theory is either ineffective or insufficiently accurate. Lattice QCD has proven to be the most powerful tool in this domain with full control on the statistical and on the systematic effects. However, traditional numerical strategies for computing the equation of state (EOS) by Monte Carlo simulations face severe limitations when extended to temperatures higher than 1 GeV or so. In particular, ultraviolet subtractions and uncertainties in the setting of the bare parameters to determine the lines of constant physics, complicate the realization of this computation and the extraction of results holding in the continuum limit.

To overcome these obstacles, we have developed novel methodologies. They combine nonperturbative renormalization techniques based on the running of a renormalized finite-volume gauge coupling up to very high energies with shifted boundary conditions in the temporal direction, allowing to directly determinate the entropy density which does not need zero-temperature subtractions. This framework allows precise simulations at high temperatures while keeping the computational cost under control and providing a simple and robust method to extrapolate the results to the continuum limit at a given physical temperature T. The approach is general and can be systematically applied to QCD with an arbitrary number of quark flavors, including heavy ones, without further theoretical adjustments.

In a recent paper [5], we reported the first nonperturbative determination of the QCD EOS up to the electroweak scale. The aim of this paper is to present in details the theoretical progress and the computational strategy that led to this result. Building on our earlier determination of the

Published by the American Physical Society under the terms of the Creative Commons Attribution 4.0 International license. Further distribution of this work must maintain attribution to the author(s) and the published article's title, journal citation, and DOI. Funded by SCOAP³.

EOS in the SU(3) Yang-Mills theory [6], we provide here the methodological foundations, numerical techniques, and consistency checks. Beyond this immediate application, these tools are of broad relevance to future lattice studies of QCD thermodynamics, including the extension to theories with four and five quark flavors and to the determination of other thermal observables, such as transport coefficients and screening masses. The tools and techniques presented in this work thus contribute to a broader effort to characterize the QCD plasma across all relevant energy scales.

The paper is organized as follows. In Sec. II we first introduce our finite temperature and shifted boundary conditions setup in the continuum, and present the main formulas for the determination of the EOS. In Sec. III we discuss the lattice discretization and the renormalization of the lattice theory. Sections IV and V are dedicated to the numerical computation of the entropy density of QCD from the lattice, and its extrapolation to the continuum limit. The full EOS of QCD is finally reported in Sec. VI where it is also compared with the results from the literature at lower temperatures and with the predictions of perturbation theory. Section VII contains our conclusions and outlook. The main text of the paper is complemented by an extensive apparatus of Appendixes where all the technical details of the new strategy proposed here are discussed.

II. THERMAL QCD AND THE EQUATION OF STATE IN THE CONTINUUM

We formulate QCD at finite temperature in the presence of shifted boundary conditions along the compact direction [7–10]. For the gauge field $A_\mu(x)$, belonging to the algebra of the gauge group SU(3), we have

$$A_\mu(x_0 + L_0, \boldsymbol{x}) = A_\mu(x_0, \boldsymbol{x} - L_0\boldsymbol{\xi}), \tag{1}$$

where L_0 is the length of the compact direction and the spatial vector $\boldsymbol{\xi} = (\xi_1, \xi_2, \xi_3)$ specifies the shift. We consider $N_f = 3$ flavors of quarks in the fundamental representation of the gauge group. The related fields are $\psi, \bar{\psi}$ and, in the compact direction, they satisfy

$$\begin{aligned} \psi(x_0 + L_0, \boldsymbol{x}) &= -\psi(x_0, \boldsymbol{x} - L_0\boldsymbol{\xi}), \\ \bar{\psi}(x_0 + L_0, \boldsymbol{x}) &= -\bar{\psi}(x_0, \boldsymbol{x} - L_0\boldsymbol{\xi}). \end{aligned} \tag{2}$$

In Euclidean spacetime, this setup describes thermal QCD in a moving reference frame characterized by the boost parameter $\boldsymbol{\xi}$. The free-energy density $f_{\boldsymbol{\xi}}$ and the partition function $\mathcal{Z}_{\boldsymbol{\xi}}$ are defined as follows:

$$f_{\boldsymbol{\xi}} = -\frac{1}{L_0 L^3} \ln \mathcal{Z}_{\boldsymbol{\xi}}, \qquad \mathcal{Z}_{\boldsymbol{\xi}} = \int DAD\bar{\psi}D\psi e^{-S_{\rm QCD}}, \tag{3}$$

where L is the size of the three spatial directions, and the thermodynamic limit $L \to \infty$ is understood. The QCD action $S_{\rm QCD}$ and the conventions for the continuum theory are specified in Appendix B of Ref. [10]. The temperature of the system is $T = 1/(L_0\sqrt{1+\boldsymbol{\xi}^2})$ and it can be varied by changing L_0 or the shift $\boldsymbol{\xi}$. Since the pressure is $p = -f_{\boldsymbol{\xi}}$, the entropy density $s = dp/dT$ can be written as [9]

$$\frac{s}{T^3} = \frac{1+\boldsymbol{\xi}^2}{\xi_k} \frac{1}{T^4} \frac{\partial f_{\boldsymbol{\xi}}}{\partial \xi_k}, \tag{4}$$

when L_0 is kept fixed. The derivative in the shift removes the additive, ultraviolet powerlike divergence in the free-energy. The pressure $p(T)$ can be obtained by integrating the entropy with respect to the temperature, while the energy density $e(T)$ follows from the thermodynamic relation $Ts = e + p$.

III. THERMAL QCD AND THE EQUATION OF STATE ON THE LATTICE

We discretize QCD on a four-dimensional hypercubic lattice of size $L_0/a \times (L/a)^3$, where a is the lattice spacing. The action of the lattice theory $S_{\rm QCD} = S_G + S_F$ is the sum of the pure gauge action S_G and the fermionic one S_F.[1] For the former we consider the Wilson plaquette discretization [11], while the latter is the nonperturbatively $O(a)$-improved Wilson-Dirac action for $N_f = 3$ degenerate quark flavors [12,13]. We refer to Appendix A for the explicit expressions. The lattice fields satisfy shifted boundary conditions along the compact direction analogous to the ones in Eqs. (1) and (2), with the field $A_\mu(x)$ replaced by the link field $U_\mu(x) \in \mathrm{SU}(3)$. Along the spatial directions they satisfy periodic boundary conditions. On the lattice, the values of the shift should satisfy the constraints $L_0\xi_k/a \in \mathbb{Z}$ and $-L/2 \le L_0\xi_k < L/2$, $k = 1, 2, 3$.

A. Renormalization and lines of constant physics

Following Ref. [14], we determine the lines of constant physics at a given temperature T by matching the value of the Schrödinger functional (SF) coupling $\bar{g}^2_{\rm SF}$ at finite lattice spacing to its value in the continuum at a scale $\mu = 1/L_0$,

$$\bar{g}^2_{\rm SF}(g_0^2, a\mu) = \bar{g}^2_{\rm SF}(\mu), \qquad a\mu \ll 1. \tag{5}$$

The right-hand side of this equation, i.e., the nonperturbative running of the renormalized coupling $\bar{g}^2_{\rm SF}(\mu)$, is known precisely in the continuum for QCD with $N_f = 3$ flavors of massless degenerate quarks [15–18]. The Eq. (5) then fixes the dependence of the bare coupling g_0 on the lattice spacing, for values of a at which the scale μ and, therefore, the temperature T can be easily accommodated. As a consequence, each temperature can be simulated at several lattice resolutions, and the continuum limit can be

[1] We use the same notation for lattice and continuum quantities, as any ambiguity is resolved from the context.

TABLE I. Second column: Physical temperatures considered in this work. Third column: Values of the Schrödinger functional coupling in $N_f = 3$ QCD at the renormalization scale $\mu = 1/L_0$.

T	T (GeV)	$\bar{g}^2_{\rm SF}(\mu = 1/L_0)$
T_0	164.6(5.6)	1.01636
T_1	82.3(2.8)	1.11000
T_2	51.4(1.7)	1.18446
T_3	32.8(1.0)	1.26569
T_4	20.63(63)	1.3627
T_5	12.77(37)	1.4808
T_6	8.03(22)	1.6173
T_7	4.91(13)	1.7943
T_8	3.040(78)	2.0120

taken with confidence. Table I reports the nine values of temperature we considered in this work, from 3 GeV up to 165 GeV. The corresponding values of the SF coupling are also shown. The critical mass $m_{\rm cr}$ at a given g_0^2 and L_0/a is then defined by requiring the PCAC mass to vanish in the SF setup. We refer to Appendix B of Ref. [14] for the technical details.

B. Entropy density on the lattice

On the lattice, at fixed bare parameters L_0/a and g_0^2, we write the entropy density in Eq. (4) as follows:

$$\frac{s}{T^3} = \frac{1+\boldsymbol{\xi}^2}{\xi_k}\frac{1}{T^4}\frac{\Delta f_{\boldsymbol{\xi}}}{\Delta \xi_k}, \tag{6}$$

where

$$\frac{\Delta f_{\boldsymbol{\xi}}}{\Delta \xi_k} = \frac{L_0}{4a}\left(f_{\boldsymbol{\xi}+\frac{2a}{L_0}\hat{k}} - f_{\boldsymbol{\xi}-\frac{2a}{L_0}\hat{k}}\right) \tag{7}$$

is the two-point symmetric discretization of the derivative of the free-energy density with respect to the kth component of the shift (see also Appendix C for further details). It is convenient from the computational viewpoint to decompose, at fixed bare parameters, the discrete derivative of the free-energy density into two contributions,

$$\frac{\Delta f_{\boldsymbol{\xi}}}{\Delta \xi_k} = \frac{\Delta f^{\infty}_{\boldsymbol{\xi}}}{\Delta \xi_k} + \frac{\Delta(f_{\boldsymbol{\xi}} - f^{\infty}_{\boldsymbol{\xi}})}{\Delta \xi_k}, \tag{8}$$

where $f^{\infty}_{\boldsymbol{\xi}}$ is the free-energy density of QCD with infinitely heavy quarks, i.e., in the static limit of QCD. We rewrite the first term as follows:

$$\frac{\Delta f^{\infty}_{\boldsymbol{\xi}}}{\Delta \xi_k} = \frac{\Delta f^{(0),\infty}}{\Delta \xi_k} + g_0^2\frac{\Delta f^{(1),\infty}}{\Delta \xi_k} - \int_0^{g_0^2} du\left(\frac{1}{u}\frac{\Delta\langle\overline{S_G}\rangle^{\infty}_{\boldsymbol{\xi}}}{\Delta \xi_k}\bigg|_{g_0^2=u} + \frac{\Delta f^{(1),\infty}}{\Delta \xi_k}\right), \tag{9}$$

where $f^{(0),\infty}$ and $f^{(1),\infty}$ represent, respectively, the tree-level and one-loop coefficients of the expansion in lattice perturbation theory of the free-energy density (see Appendix B) computed at infinite bare quark masses. The discrete derivatives in the shift are defined analogously to Eq. (7), and

$$\langle\overline{S_G}\rangle^{\infty}_{\boldsymbol{\xi}} = \frac{a^4}{L_0 L^3}\langle S_G\rangle^{\infty}_{\boldsymbol{\xi}} \tag{10}$$

is the expectation value of the pure gauge action density in the static quark limit and in the shifted setup. The second contribution to Eq. (8) can be rewritten as

$$\frac{\Delta(f_{\boldsymbol{\xi}} - f^{\infty}_{\boldsymbol{\xi}})}{\Delta \xi_k} = -\frac{\Delta}{\Delta \xi_k}\int_0^{\infty} dm_q \frac{\partial f^{m_q}_{\boldsymbol{\xi}}}{\partial m_q} = -\int_0^{\infty} dm_q \frac{\Delta\langle\bar{\psi}\psi\rangle^{m_q}_{\boldsymbol{\xi}}}{\Delta \xi_k}, \tag{11}$$

where $m_q = m_0 - m_{\rm cr}(g_0^2, L_0)$ is the bare subtracted quark mass and $\langle\bar{\psi}\psi\rangle^{m_q}_{\boldsymbol{\xi}}$ is the expectation value of the scalar density at a given subtracted quark mass. Again, the discrete derivative with respect to the shift is defined similarly to Eq. (7).

IV. NUMERICAL COMPUTATION

In the following we discuss the numerical evaluation on the lattice of the two contributions in Eqs. (9) and (11). At each given temperature we have considered four resolutions $L_0/a = 4, 6, 8, 10$ of the compact direction, while the three spatial directions are of the same size $L/a = 144$; the aspect ratio LT of our lattices thus ranges between 10 and 25. The choice of the shift is to some extent arbitrary, and can be leveraged for a good compromise between discretization effects and relative accuracy of the entropy density, as we discuss in Appendix C. The chosen value in this work is $\boldsymbol{\xi} = (1, 0, 0)$. At a given temperature and L_0/a, the values of the inverse bare coupling, of the critical hopping parameter and of the nonperturbative $O(a)$-improvement coefficient can be found in Table 4 of Ref. [14].

A. Numerical determination of $\frac{\Delta f^{\infty}_{\boldsymbol{\xi}}}{\Delta \xi_k}$

We computed the contribution $\frac{\Delta f^{\infty}_{\boldsymbol{\xi}}}{\Delta \xi_k}$ by estimating the integral in the bare coupling of Eq. (9) using an optimized combination of numerical quadratures. A similar integration has been employed in Ref. [19], where it was shown that the integrand function is smooth in g_0^2 in the interval of interest, and that any systematic effects arising from the numerical quadratures are negligible with respect to the statistical accuracy of the integral. At a given L_0/a and for each value of g_0^2 prescribed by the chosen quadrature rules, we have measured $\langle\overline{S_G}\rangle^{\infty}_{\boldsymbol{\xi}}$ in simulations of the pure SU(3) Yang-Mills theory in the shifted setup, at the values $\boldsymbol{\xi} = (1 \pm 2a/L_0, 0, 0)$ required by the computation of the discrete derivative with respect to the shift. The integral

TABLE II. Summary of the integration scheme for the computation of the integral in g_0^2 appearing in Eq. (9).

Interval	Quadrature	
$0 \le g_0^2 \le 6/15$	3 (Simpson) 2 (Trapezoid)	$L_0/a = 4$ $L_0/a = 6,\ 8,\ 10$
$6/15 \le g_0^2 \le 6/9$	3 (Gauss-Legendre)	
$6/9 \le g_0^2 \le g_0^2\|_{T_0}$	3 (Gauss-Legendre) 1 (Midpoint)	$L_0/a = 4$ $L_0/a = 6$
$6/9 \le g_0^2 \le g_0^2\|_{T_1}$	3 (Gauss-Legendre)	
$g_0^2\|_{T_{i-1}} \le g_0^2 \le g_0^2\|_{T_i}$	3 (Gauss-Legendre) 5 (Gauss-Legendre)	$1 < i < 7$ $i = 7, 8$

in the bare coupling is then obtained from the linear combination of these results, with weights that are uniquely determined by the quadrature rules and the integration intervals.

At fixed L_0/a, the integration in the bare coupling has to be performed in the intervals $g_0^2 \in [0, g_0^2|_{T_i}]$, $i = 0, 1, \ldots, 8$, where $g_0^2|_{T_i}$ is the bare coupling squared at the given temperature T_i whose corresponding inverse values $6/g_0^2$ are reported in Table III. We have computed first the integral for the value of g_0^2 associated to the temperature T_1 by splitting the integration in three domains as follows:

$$\int_0^{g_0^2|_{T_1}} du(\bullet) = \int_0^{6/15} du(\bullet) + \int_{6/15}^{6/9} du(\bullet) + \int_{6/9}^{g_0^2|_{T_1}} du(\bullet), \tag{12}$$

where the dot stands for the integrand function of Eq. (9). For $L_0/a = 4, 6$ we have one further temperature, T_0, whose integral is computed as in Eq. (12) by replacing $g_0^2|_{T_1}$ with $g_0^2|_{T_0}$. At the lower temperatures ($i > 1$), the integral is then obtained by adding to the result at temperature T_{i-1} the integral in the domain $g_0^2 \in [g_0^2|_{T_{i-1}}, g_0^2|_{T_i}]$,

$$\int_0^{g_0^2|_{T_i}} du(\bullet) = \int_0^{g_0^2|_{T_{i-1}}} du(\bullet) + \int_{g_0^2|_{T_{i-1}}}^{g_0^2|_{T_i}} du(\bullet). \tag{13}$$

A summary of the integration scheme can be found in Table II.[2] The first column reports the integration domains, and the second column the respective quadrature rules and number of integration points for the different values of L_0/a and temperatures. A showcase of the numerical results for $\frac{\Delta\langle\overline{S_G}\rangle_\xi^\infty}{\Delta\xi_k}$ is given in Table XI of Appendix H for $L_0/a = 6$ together with the values of inverse bare coupling

[2]Note that the integration starting from $g_0^2 = 0$ is carried out up to values of the bare coupling well-below the critical point where the first order transition of the SU(3) pure gauge theory occurs, see e.g., Ref. [20].

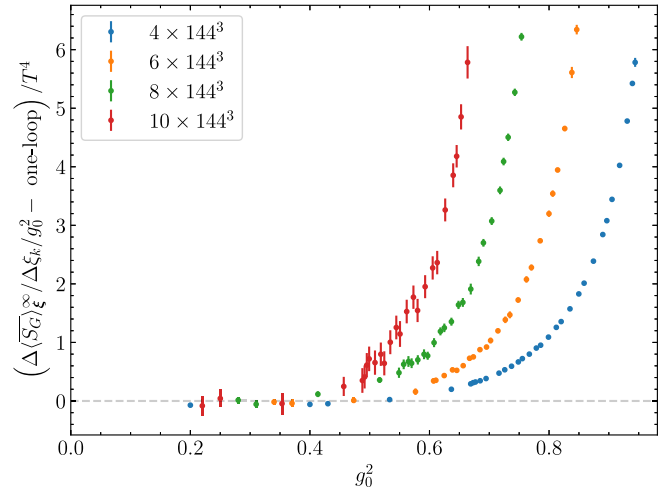

FIG. 1. Plot of the integrand function in Eq. (9) as a function of the bare coupling g_0^2. Points have been shifted horizontally by $0.03 \times (L_0/a - 4)$ for better readability.

$6/g_0^2$. The integrand function of Eq. (9) is shown in Fig. 1 for the four lattice resolutions $L_0/a = 4, 6, 8, 10$.

The pure gauge ensembles for this computation have been generated by Monte Carlo simulations where the basic sweep is a combination of heat bath and over-relaxation [21] updates of the link variables, using the Cabibbo-Marinari scheme [22–24]. We collected about 6000 measurements of S_G per quadrature point (about 3000 per shift) for $L_0/a = 4, 6$ and about 40000 measurements per quadrature point for the two finest resolutions $L_0/a = 8, 10$. The final results for $\frac{\Delta f_\xi^\infty}{\Delta\xi_k}$ at fixed lattice spacing are reported in Table II of Ref. [5] and they have relative errors of a few permille for $L_0/a = 4$, 6, about 0.5% for $L_0/a = 8$ and about 1.5% for $L_0/a = 10$.

B. Numerical determination of $\frac{\Delta(f_\xi - f_\xi^\infty)}{\Delta\xi_k}$

We now describe the numerical strategy for the computation of the integral in the bare quark mass that defines the contribution $\frac{\Delta(f_\xi - f_\xi^\infty)}{\Delta\xi_k}$ to the QCD entropy density through Eq. (11). We split the integral in three parts,

$$\int_0^\infty dm_q \frac{\Delta\langle\bar\psi\psi\rangle_\xi^{m_q}}{\Delta\xi_k} = T\int_0^5 d\tilde m_q(\bullet) + T\int_5^{\tilde m} d\tilde m_q(\bullet) + T\int_{\tilde m}^\infty d\tilde m_q(\bullet), \tag{14}$$

where $\tilde m_q = m_q/T$ and $\tilde m = 35$ for $L_0/a = 4$ or $\tilde m = 20$ for $L_0/a = 6, 8, 10$. We have chosen a ten-point Gauss quadrature for the first domain and a seven-point Gauss quadrature for the second domain (six-point Gauss quadrature for $L_0/a = 6$, $6/g_0^2 = 8.5403$). We have integrated the third domain with a three-point Gauss quadrature, after a change of integration variable to the hopping parameter,

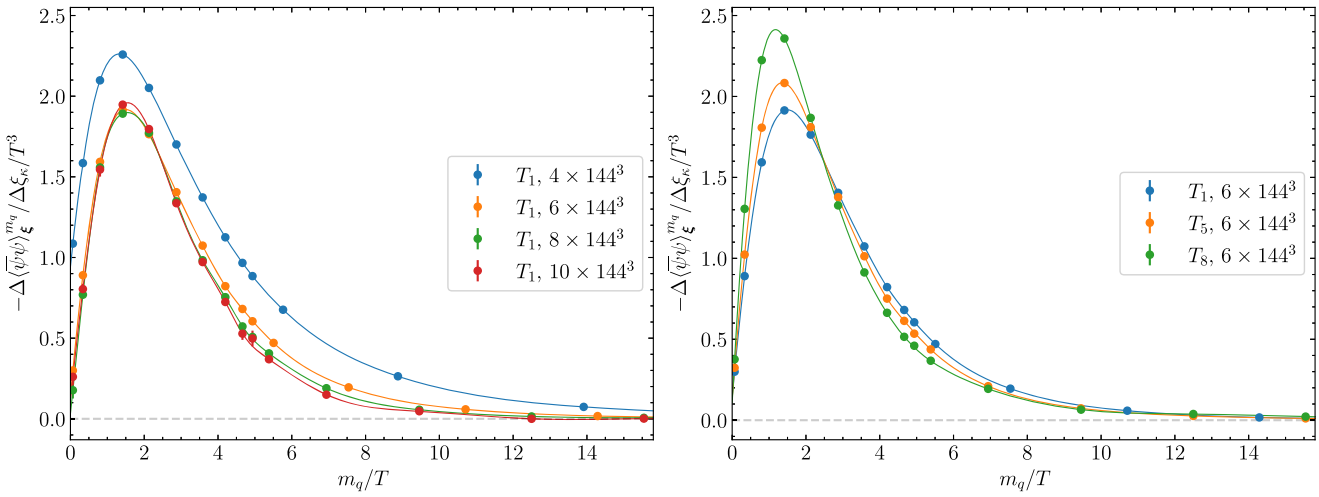

FIG. 2. Left: Plot of the integrand function in Eq. (11) computed at the bare parameters of temperature T_1 and at the resolutions $L_0/a = 4, 6, 8, 10$, as a function of m_q/T. Points have been interpolated with a cubic spline to guide the eye. In most cases, errors are smaller than the markers. Right: The same integrand function is shown at the resolution $L_0/a = 6$ and at three temperatures.

$$\kappa = \frac{1}{2(aT\tilde{m}_q + am_{\rm cr} + 4)}, \tag{15}$$

which makes this integration interval compact. As explained in Appendix D, this optimized integration scheme guarantees that any systematic error introduced by the numerical quadratures is negligible with respect to the statistical accuracy of the nonperturbative results. The nonperturbative integrand function is represented in Fig. 2 for different values of the lattice spacing (left panel) and different temperatures (right panel); we report in Table XII the numerical results of $\frac{\Delta\langle\bar{\psi}\psi\rangle_{\xi}^{m_q}}{\Delta\xi_k}$ at some representative values of the bare parameters.

The nonperturbative results for $\frac{\Delta(f_\xi - f_\xi^\infty)}{\Delta\xi_k}$ at given L_0/a and g_0^2 are collected in Table II of Ref. [5]. The numerical determination of each of them requires to simulate QCD at the 20 values of bare quark mass prescribed by the nodes of the Gauss quadratures, for the two shifts $\boldsymbol{\xi} = (1 \pm 2a/L_0, 0, 0)$ giving a total of 40 independent simulations. Taking advantage of the peculiarities of the quantity of interest, we managed to highly optimize the numerical approach in order to minimize the computational effort. We summarize these aspects in the following, and refer to dedicated Appendixes for more details.

1. Simulating at large quark masses

The values of bare subtracted quark mass in our QCD simulations range between the chiral limit $m_q = 0$ and the static quark limit $m_q \to \infty$. The heavier the quarks, the less they contribute to the dynamics; this allows us to treat the fermionic forces in the molecular dynamics of the hybrid Monte Carlo (HMC) with coarser integration schemes as we increase the bare quark mass, with small impact on the acceptance rate. By scrutinizing in detail the magnitude of the fermionic forces and the spectral gap of the Dirac operator for increasing values of the bare quark mass, we selected four optimal algorithms for the molecular dynamics which maximize the acceptance rate (always above 90%) of the HMC while minimizing the computational cost. The description of the chosen algorithms, of the tuning procedure and of the generation of our QCD ensembles can be found in Appendix E.

2. Variance reduction

The primary quantity for the numerical determination of $\frac{\Delta(f_\xi - f_\xi^\infty)}{\Delta\xi_k}$ is the expectation value of the scalar density, $\langle\bar{\psi}\psi\rangle_{\xi}^{m_q}$, to be computed in QCD simulations with increasing values of the bare quark mass. To profit from translational invariance, at fixed gauge configuration we have employed U(1) random sources for the computation of the trace of the quark propagator. Following Ref. [25] we have introduced an improved estimator of the latter, obtained by subtracting its leading nontrivial order in the hopping parameter expansion. This significantly reduces the contribution to the variance due to the random sources with respect to the naive estimator, with an overall gain up to a factor 2.5 in the statistical error of $\frac{\Delta(f_\xi - f_\xi^\infty)}{\Delta\xi_k}$ at negligible additional computational effort. The details of this procedure are reported in Appendix F.

3. Optimization of the statistics

At fixed parameters L_0/a and g_0^2, the uncertainty of the contribution $\frac{\Delta(f_\xi - f_\xi^\infty)}{\Delta\xi_k}$ is propagated from the one of $\langle\bar{\psi}\psi\rangle_{\xi}^{m_q}$, which is measured in independent numerical simulations at the different values of the bare quark mass prescribed by the Gauss quadratures. The different magnitude of the Gauss weights and the dependence of the variance of the

TABLE III. Results at fixed bare parameters of the derivative in the shift of the free-energy density.

L_0/a	$6/g_0^2$	$\frac{\Delta f_\xi}{\Delta \xi_k} \times 10^4$	$6/g_0^2$	$\frac{\Delta f_\xi}{\Delta \xi_k} \times 10^4$	$6/g_0^2$	$\frac{\Delta f_\xi}{\Delta \xi_k} \times 10^4$
	T_0		T_1		T_2	
4	8.7325	149.05(4)	8.3033	148.29(5)	7.9794	147.55(6)
6	8.9950	22.07(6)	8.5403	21.92(4)	8.2170	21.96(4)
8	⋯	⋯	8.7325	6.448(26)	8.4044	6.443(23)
10	⋯	⋯	8.8727	2.596(21)	8.5534	2.581(22)
	T_3		T_4		T_5	
4	7.6713	146.87(6)	7.3534	146.07(6)	7.0250	144.93(6)
6	7.9091	21.80(5)	7.5909	21.72(5)	7.2618	21.58(5)
8	8.0929	6.388(25)	7.7723	6.389(26)	7.4424	6.403(29)
10	8.2485	2.567(22)	7.9322	2.597(23)	7.6042	2.550(26)
	T_6		T_7		T_8	
4	6.7079	143.80(7)	6.3719	142.32(9)	⋯	⋯
6	6.9433	21.50(5)	6.6050	21.38(6)	6.2735	21.14(7)
8	7.1254	6.326(23)	6.7915	6.32(4)	6.4680	6.30(4)
10	7.2855	2.577(26)	6.9453	2.562(23)	6.6096	2.511(26)

scalar density estimator with the bare quark mass (see Appendix F) make the Gauss points contribute differently to the final error. The computational effort changes with the bare quark mass too, and it is possible to tune the statistics for $\langle \bar{\psi}\psi \rangle_{\boldsymbol{\xi}}^{m_q}$ at each Gauss point such that the total computational cost is minimized given a target precision for $\frac{\Delta(f_\xi - f_\xi^\infty)}{\Delta \xi_k}$. This optimization has been performed for a target relative error of 0.5% for $L_0/a = 4, 6, 8$, and 1% for $L_0/a = 10$. Further details on this procedure can be found in Appendix G, where the optimized number of measurements is reported. This optimization led to a final gain up to a factor 2 in the computational time compared to the case where, at fixed target accuracy, the same statistics is considered for all the Gauss points.

V. ENTROPY DENSITY

The results discussed in this section correspond to those reported in Ref. [5], where the EOS of $N_f = 3$ QCD was determined nonperturbatively. Here, we provide the full details of the continuum extrapolation and of the fit strategy adopted.

At fixed L_0/a and g_0^2, the derivative of the free-energy density with respect to the shift, $\frac{\Delta f_\xi}{\Delta \xi_k}$, is obtained by summing the two contributions $\frac{\Delta f_\xi^\infty}{\Delta \xi_k}$ and $\frac{\Delta(f_\xi - f_\xi^\infty)}{\Delta \xi_k}$ determined as described in Sec. IV; the final results are reported in Table III. The entropy density then follows from Eq. (6). In propagating the errors from the primary observables to the entropy density, we have accounted for correlations using the gamma method [26], as implemented in Refs. [27,28]. We have also included the systematic uncertainty coming from the definition of the lines of constant physics [14,16], even though its contribution is negligible within the final accuracy.

A. Finite volume effects

On general grounds, finite volume effects in QCD are exponentially suppressed as $e^{-M_{\rm gap} L}$, where $M_{\rm gap}$ is the mass gap of the theory and L is the linear spatial size of the system. In the high-temperature regime under investigation, $M_{\rm gap}$ corresponds to the mass of the lightest screening state, which scales proportionally to T with a coefficient close to unity [9,14,29]. Since in our simulations $10 \lesssim LT \lesssim 25$, finite size effects are expected to be negligible compared to the statistical accuracy of our numerical results.

In order to validate this expectation, in Ref. [5] we presented a comparison of nonperturbative results from lattices with spatial sizes $L/a = 144$ and $L/a = 288$ at some selected bare parameters. Instead of computing the entropy density from the derivative of the free-energy density, we used the one-point function of the energy-momentum tensor [9]. This provides an alternative discretization of the entropy density,

$$\frac{s}{T^3} = -\frac{1+\boldsymbol{\xi}^2}{\xi_k} \frac{1}{T^4} \langle T_{0k}^{R,\{6\}} \rangle_{\boldsymbol{\xi}}, \tag{16}$$

equivalent to Eq. (6) up to cutoff effects. In Eq. (16) the sextet components of the renormalized energy-momentum tensor,

$$T_{\mu\nu}^{R,\{6\}} = Z_G^{\{6\}}(g_0^2) T_{\mu\nu}^{G,\{6\}} + Z_F^{\{6\}}(g_0^2) T_{\mu\nu}^{F,\{6\}}, \tag{17}$$

are defined as in Sec. 3 of Ref. [10]. At present, the entropy density cannot be determined nonperturbatively from Eq. (16) because the renormalization constants $Z_G^{\{6\}}$ and

$Z_F^{\{6\}}$ are known only at one-loop order in bare lattice perturbation theory. However, since the latter are insensitive to finite volume effects, the matrix elements $\langle T_{\mu\nu}^{G,\{6\}}\rangle_\xi$ and $\langle T_{\mu\nu}^{F,\{6\}}\rangle_\xi$ can be used as a proxy to study the finite volume effects affecting the entropy density. Their lattice determination is significantly less demanding than the computation of the entropy via Eq. (6).

We computed the bare matrix elements on 6×144^3 and 6×288^3 lattices, with a statistical precision such that the relative error on s/T^3 as in Eq. (16) is comparable to that obtained from the results in Table III. The renormalization constants $Z_G^{\{6\}}$ and $Z_F^{\{6\}}$, appearing in Eq. (17), have been estimated using perturbation theory at one-loop order [10]. We carried out this study at the temperatures T_1, T_8, and no finite volume effects were observed in the matrix elements (see Table III in Ref. [5]). This makes us confident that, for $10 \lesssim LT \lesssim 25$, they are negligible on the entropy density at all the temperatures considered in this work.

B. Restricting to zero topological sector

In the interval of temperatures that we have investigated, 3 GeV $\lesssim T \lesssim$ 165 GeV, the trivial topological sector of the QCD phase space gives by far the dominant contribution to the path integral. At asymptotically high temperatures, the instanton analysis predicts the topological susceptibility to be suppressed as $\sim T^{-b}m^3$, $b\sim 8$, for QCD with three light degenerate quark flavors of mass m. The analogous prediction for the pure SU(3) gauge theory has been explicitly verified nonperturbatively [30]. Similarly, lattice QCD calculations tend to confirm the scaling with T predicted in the semiclassical analysis, even though the systematics introduced by dynamical fermions is still difficult to control [31]. For all practical purposes, we can compute the entropy density by restricting our main observables, $\langle\overline{S_G}\rangle_\xi^\infty$ and $\langle\bar\psi\psi\rangle_\xi^{m_q}$, to the trivial topological sector. The systematics introduced by neglecting nonzero topological sectors is much below the statistical accuracy of our numerical results.

In our pure gauge ensembles we have however observed some topological activity for bare couplings between $g_0^2|_{T_7}$ and $g_0^2|_{T_8}$ for $L_0/a = 6, 8, 10$ and for $6/g_0^2 \lesssim 6.5$ when $L_0/a = 4$. In the QCD simulations, nonvanishing topological sectors occurred only in $L_0/a = 4$, 6 ensembles at temperatures T_7, T_8 and for values of the hopping parameter $\kappa \lesssim 0.10$, where the topological susceptibility is expected to be less suppressed. We have computed the expectation values of the Wilson plaquette action and of the scalar density restricting the integration in various topological sectors, and no difference can be observed within statistical errors. This result is in agreement with other studies at lower temperatures [32]. So as to be the most conservative, we added a systematic error to $\langle\overline{S_G}\rangle_\xi^\infty$ for data between T_7 and T_8 up to a total relative error of 2%, in order to safely take into account any effect from the observed topological fluctuations.

TABLE IV. Coefficients for improvement of the lattice entropy density at one-loop order. The last column corresponds to the continuum values appearing in Eq. (18).

a/L_0	1/4	1/6	1/8	1/10	0
$\frac{1}{T^4}\frac{\Delta f^{(0)}}{\Delta\xi_k}$	16.561	12.065	11.036	10.736	10.418
$\frac{1}{T^4}\frac{\Delta f^{(1)}}{\Delta\xi_k}$	−2.086	−1.163	−0.885	−0.808	−0.750

C. Continuum limit

Improved definitions of observables reduce the systematic effects of lattice artifacts when performing the extrapolation to the continuum limit of results obtained at finite lattice spacing. For the entropy density we have considered the following improved definition:

$$s\left(\frac{a}{L_0}, g_0^2\right) \to s\left(\frac{a}{L_0}, g_0^2\right)\frac{\frac{\partial}{\partial\xi_k}[f_0 + g^2 f_1]}{\frac{\Delta}{\Delta\xi_k}[f^{(0)} + g^2 f^{(1)}]}, \quad (18)$$

where $g = \bar g_{\rm SF}(1/L_0)$, f_0 and f_1 are the tree-level and one-loop perturbative coefficients of the free-energy density in the continuum while $f^{(0)}$, $f^{(1)}$ are the corresponding coefficients computed in lattice perturbation theory [10], summarized in Appendix B. Table IV contains the results at fixed lattice spacing and in the continuum limit relevant for the improvement at one-loop order. Using Eq. (18), discretization effects at tree level and $O(g^2)$ are subtracted from our observable to all orders in the lattice spacing.

We have extrapolated to the continuum limit the one-loop improved lattice results for the entropy density by a global fit of the data to all temperatures. We have parametrized the temperature dependence of the discretization effects in terms of polynomials of a renormalized coupling, and the natural choice is the nonperturbative SF coupling used to define the lines of constant physics. Since the lattice theory is $O(a)$-improved, and since at finite temperature odd powers in the coupling are generally present, after the improvement at one-loop order the leading discretization effects of the lattice results are expected to be of order $O(a^2g^3)$. Thus, we considered the following general fit function:

$$s(T_i, a/L_0)/T_i^3 = c_i + \left(\frac{a}{L_0}\right)^2(d_{23}g_i^3 + d_{24}g_i^4) + \left(\frac{a}{L_0}\right)^3(d_{33}g_i^3 + d_{34}g_i^4), \quad (19)$$

where $i = 0, \ldots, 8$ and $g_i = \bar g_{\rm SF}(\sqrt{2}T_i)$. The fit parameters c_i are the continuum results for s/T^3 at the different temperatures $T_0, \ldots, T_8$, while the d_{ij} parametrize the discretization effects. We explored a variety of fits to assess the

TABLE V. Summary of the results of the fits that we considered for the extrapolation of s/T^3 to the continuum limit. Each column of the table corresponds to a fit, labeled for convenience by the `id` number in the first row. The second row tells which lattice spacings have been included in the fit. The third row indicates if a systematic error arising from the indicated cutoff effects has been added in quadrature to the statistical error of the numerical results, see main text for details. The remaining rows report the fitted parameters and the value of $\chi^2/\chi^2_{\rm exp}$.

	id0	id1	id2	id3 (best-fit)	id4	id5	id6
L_0/a	4, 6, 8, 10	4, 6, 8, 10	6, 8, 10	6, 8, 10	6, 8, 10	6, 8, 10	6, 8, 10
syst				a^3g^3	a^3g^3	a^4g^3	a^3g^4
c_0	20.057(22)	20.00(8)	20.10(7)	20.13(8)	20.14(11)	20.11(7)	20.15(6)
c_1	20.031(25)	19.97(9)	20.01(6)	20.05(8)	20.06(11)	20.01(7)	20.05(6)
c_2	19.996(28)	19.93(10)	20.04(7)	20.05(9)	20.06(11)	20.04(7)	20.07(7)
c_3	19.97(3)	19.89(11)	19.90(7)	19.90(9)	19.91(11)	19.90(8)	19.92(8)
c_4	19.94(3)	19.86(12)	19.88(8)	19.93(10)	19.93(11)	19.89(9)	19.92(9)
c_5	19.88(4)	19.79(13)	19.81(9)	19.87(11)	19.87(11)	19.82(10)	19.86(10)
c_6	19.84(4)	19.73(15)	19.73(10)	19.75(12)	19.75(12)	19.73(10)	19.73(11)
c_7	19.80(5)	19.67(18)	19.69(12)	19.74(15)	19.73(15)	19.70(13)	19.70(14)
c_8	19.63(7)	19.48(22)	19.53(14)	19.58(17)	19.56(20)	19.55(15)	19.51(17)
d_{23}	5.5(3)	10(7)	6.9(1.9)	6(4)	3(16)	6.7(2.4)	
d_{24}					2(12)		5.1(2.5)
d_{33}		−15(22)					
$\chi^2/\chi^2_{\rm exp}$	1.06	1.12	0.74	0.82	0.85	0.76	0.80

cutoff effects and ensure that systematic uncertainties from the extrapolation were well under control. We report on the more representative fits, which are also summarized in Table V, each labeled with an `id` number.

We first considered fits without $O(g^4)$ terms by enforcing $d_{24} = d_{34} = 0$. We fitted data with $L_0/a = 4, 6, 8, 10$ by setting either $d_{33} = 0$ (fit `id0`) or $d_{33} \neq 0$ (fit `id1`). While both fits have $\chi^2/\chi^2_{\rm exp} \approx 1$, with $\chi_{\rm exp}$ defined as in Ref. [33], fit `id0` gives continuum values c_i with errors 3–4 times smaller. Although compatible within the larger errors of fit `id1`, the extrapolated central values of the first fit are systematically higher.

A quadratic fit of the lattice artifacts excluding the data at $L_0/a = 4$ yields $\chi^2/\chi^2_{\rm exp} = 0.74$ (fit `id2`). This fit provides estimates of the continuum values that are in good agreement with fit `id1`, both in terms of central values and error size. This suggests that the data at $L_0/a = 4$ are likely affected by discretization effects of higher order than a^2. Thus, we used the data at the coarsest lattice spacing only to estimate the size of the $O(a^3)$ contributions and included these as a systematic error for the $L_0/a = 6, 8, 10$ data.

More specifically, we used the value of d_{33} obtained from the fit `id1` as an estimate of the systematic uncertainty and we added it in quadrature to the statistical errors, $\sigma(T_i, a/L_0)$, of s/T^3 at given temperature and lattice spacing,

$$\sigma^2\left(T_i, \frac{a}{L_0}\right) \to \sigma^2\left(T_i, \frac{a}{L_0}\right) + \left[\left(\frac{a}{L_0}\right)^3 d_{33} g_i^3\right]^2. \quad (20)$$

The final best-fit is the one considering data with $L_0/a > 4$, $d_{24} = d_{33} = d_{34} = 0$ in the fit ansatz Eq. (19), and errors as in Eq. (20) for the definition of the weights in the χ^2 function minimized by the fit. This fit is labeled `id3` in Table V. The continuum results for the normalized entropy density have a relative error of 0.5%–1.0%, and their covariance matrix can

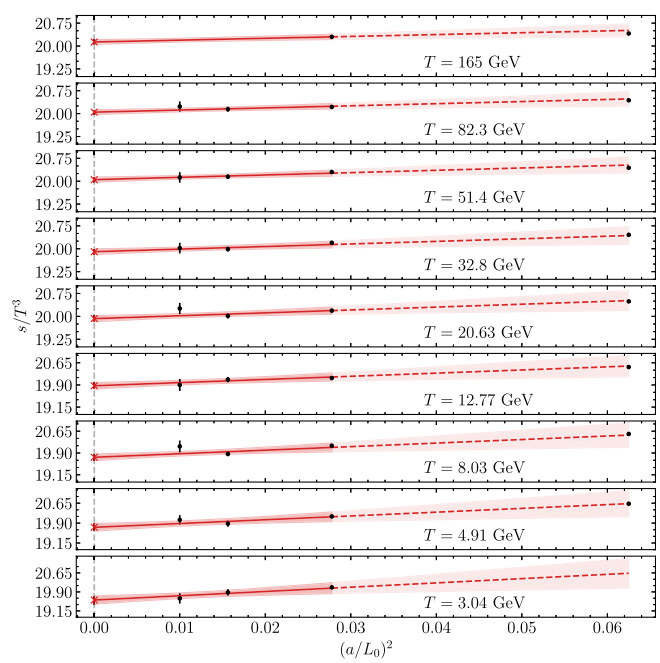

FIG. 3. Black dots are the values of the one-loop improved normalized entropy density as a function of $(a/L_0)^2$ at the temperatures $T_0, T_1, \ldots, T_8$. The red band is our best extrapolation to the continuum limit (fit `id3` in Table V). Red crosses are the continuum extrapolated values for s/T^3. The horizontal axis is common to all the subplots.

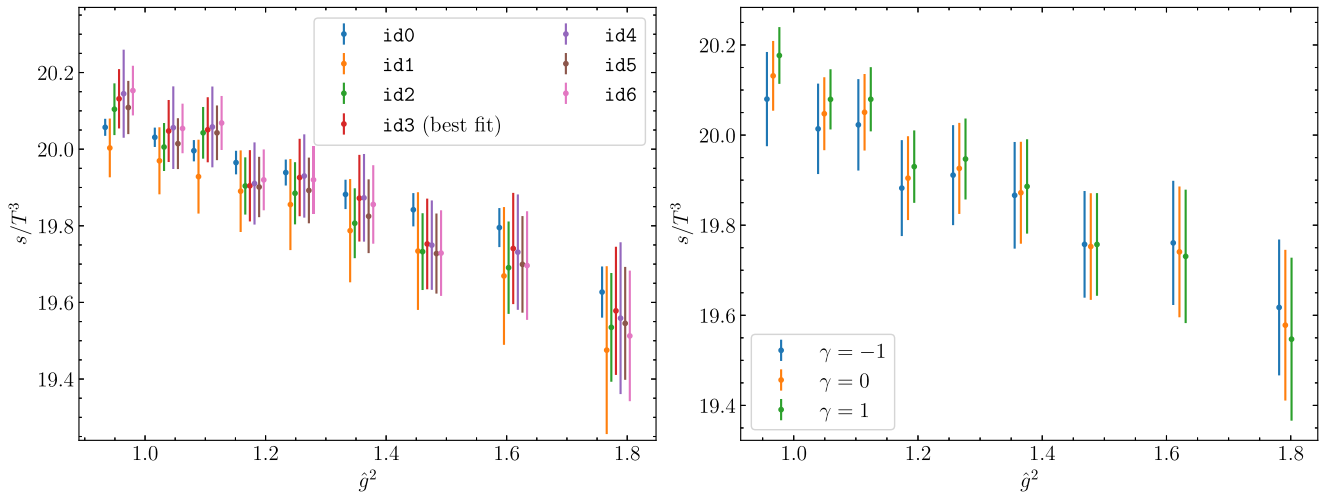

FIG. 4. Left: Comparison among the results of different continuum limits. Points have been shifted horizontally by $0.023 \times (n/3 - 1)$ where $n = 0, 1, \ldots, 6$ for fits `id0`, `id1`, ..., `id6`. Right: Effect of logarithmic corrections on the continuum extrapolated values of the best-fit. For better readability points have been shifted horizontally by $0.01 \times \gamma$, with γ defined in Eq. (22).

be found in Appendix H. Figure 3 shows the related continuum extrapolation.

We performed several checks to further corroborate the robustness of our best-fit. We first repeated the best-fit letting $d_{24} \neq 0$ in Eq. (19). The continuum limits of this fit `id4` are perfectly compatible to those of the best-fit, meaning that the parametrization of the cutoff effects is not sensitive (within errors) to the inclusion of higher powers of the renormalized coupling. We also repeated the whole analysis considering subleading cutoff effects of $O(a^4)$ instead of $O(a^3)$ in the fit ansatz and in Eq. (20). The resulting c_i (fit `id5`) are stable with respect to the best-fit, with errors that are 10%–20% smaller. Similar conclusions hold when, in the cutoff effects, the leading power of the coupling is chosen to be $O(g^4)$ instead of $O(g^3)$ in both the fit ansatz and in the determination of the systematic error (fit `id6`).

The continuum results from all these fits are actually well compatible with each other as shown in the left panel of Fig. 4. In the latter, data have been plotted against the renormalized coupling squared $\hat{g}^2$, defined as the five-loop $\overline{\mathrm{MS}}$ coupling [34] at the renormalization scale $\mu = 2\pi T$, whose leading-order expression is

$$\frac{1}{\hat{g}^2(\mu)} = \frac{9}{8\pi^2} \ln \frac{\mu}{\Lambda_{\overline{\mathrm{MS}}}} + \ldots, \qquad \mu = 2\pi T, \tag{21}$$

where $\Lambda_{\overline{\mathrm{MS}}} = 341$ MeV is taken from Ref. [17]. For our purposes, this is only a convenient function of T that we choose to study the temperature dependence of our nonperturbative results. Further details on the computation of $\hat{g}$ are reported in Appendix I.

We finally checked the impact of logarithmic corrections to the leading discretization effects, of $O(a^2 g^3)$, on the best-fit `id3` using the modified fit ansatz [35–37],

$$s(T_i, a/L_0)/T_i^3 = c_i + d_{23}[\bar{g}^2_{\mathrm{SF}}(\pi/a)]^\gamma \left(\frac{a}{L_0}\right)^2 g_i^3, \tag{22}$$

where $\bar{g}_{\mathrm{SF}}(\pi/a)$ is the renormalized SF coupling evaluated at the cutoff scale. The continuum results of s/T^3 change by less than one standard deviation with respect to the best-fit, $\gamma = 0$, when the effective anomalous dimension is varied in the interval $\gamma \in [-1, 1]$. The comparison for three selected values of γ is shown in the right panel of Fig. 4.

VI. EQUATION OF STATE

The main nonperturbative results are the values of the normalized entropy density s/T^3 of continuum QCD reported in Table V with the fit label `id3`, corresponding to the nine temperatures from 3 to 165 GeV of Table I. These values are shown as black dots in Fig. 5 as a function of the strong coupling squared $\hat{g}^2$ defined above. These results can be fitted to obtain an analytic expression for the temperature dependence of the entropy density, and thus for the other thermodynamic functions in the EOS, namely the pressure and the energy density.

A. Temperature dependence of the entropy density

We have parametrized the temperature dependence of the entropy density in terms of a polynomial in the renormalized coupling $\hat{g}$,

$$\frac{s}{T^3} = \frac{32\pi^2}{45} \sum_k s_k \left(\frac{\hat{g}}{2\pi}\right)^k. \tag{23}$$

This convenient choice allows us to more easily compare our nonperturbative results with the predictions of perturbation theory. This study has been carried out in Ref. [5]; we report in Table VI the results for the fits which are relevant for the discussion in the following. The first fit has

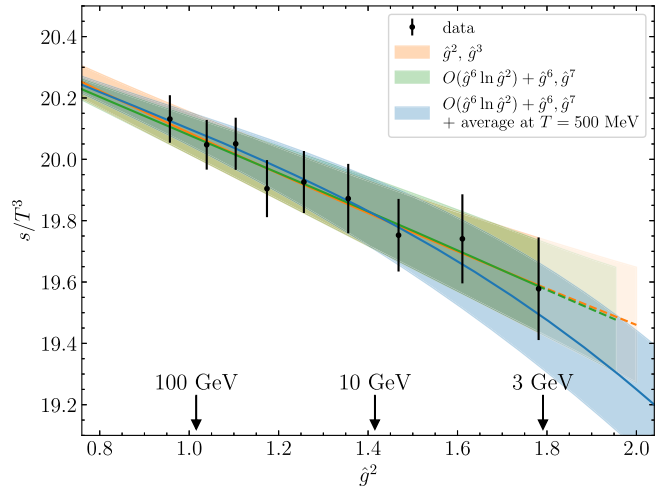

FIG. 5. Comparison of the three parametrizations of the temperature dependence of s/T^3, in the temperature interval covered by the nonperturbative data.

been performed by enforcing the Stefan-Boltzmann result at infinite temperature, $s_0^{\rm SB} = 2.969$, and taking the coefficients s_2, s_3 as fit parameters. This fit is shown in Fig. 5 as the orange shadowed band.

In the second fit we have enforced all the known coefficients in perturbation theory up to $O(\hat{g}^6 \ln \hat{g}^2)$ [38–45] so as to constrain the parametrization in the asymptotically high-temperature regime. We have fitted to the data the unknown term at $O(\hat{g}^6)$ and one further term of $O(\hat{g}^7)$ to take into account any higher-order effects in the expansion in $\hat{g}$. The green band in Fig. 5 shows this fit. The fitted coefficients actually include the nonperturbative contribution of the ultrasoft modes [46,47] and a not yet known perturbative term. The determination of the missing perturbative coefficient at $O(\hat{g}^6)$ (see Ref. [48] for recent progresses) would allow us to disentangle the ultrasoft effects and estimate the relative magnitude.

The third fit ansatz is the same as the second, but we included in the nonperturbative dataset the value $s/T^3 = 17.31(16)$ at $T = 500$ MeV coming from the weighted average of the results from Refs. [32,49,50], obtained in $N_f = 2 + 1$ QCD. This procedure is consistent as the effect of the quark masses at $T = 500$ MeV is several times smaller than the error on the entropy density quoted by the two collaborations [51]. This fit is our best parametrization of the entropy density of $N_f = 3$ QCD for $T \geq 500$ MeV, and it is represented in Fig. 5 (blue band) and in the left panel of Fig. 7. Figure 5 shows that all these parametrizations are perfectly compatible in the whole temperature range from 3 to 165 GeV covered by the nonperturbative results, both in the central values and in the error bands.

B. Comparison with perturbation theory

We now compare our nonperturbative results for the normalized entropy density with the analytic results in standard perturbation theory and in hard thermal loop perturbation theory [52–54].

The curves of the perturbative expansion for s/T^3 are shown in the left panel of Fig. 6, each including all the orders up to $O(\hat{g}^k)$, $k = 2, 3, \ldots, 6$ as indicated by the labels. The shadowed bands correspond to varying the renormalization scale by the factors 0.5 and 2 with respect to $\mu = 2\pi T$. We have also propagated the statistical uncertainty on the nonperturbative $\Lambda_{\overline{\rm MS}}$ [17], but the related contribution is completely subdominant. The curves at $O(\hat{g}^k)$ and $O(\hat{g}^{k+1})$ with $k = 2, 3, 4, 5$ in Fig. 6 are in tension by a few combined standard deviations, with the exception of the $k = 3$ case which shows some agreement for $T \lesssim 100$ GeV. Therefore, in the temperature interval under investigation, higher order effects in the perturbative expansion are relevant and the convergence is slow. This is also signaled by the fact that, in our best parametrization (third column of Table VI), the contributions beyond the known perturbative expansion at $T \sim 165$ GeV still give about 40% of the interactions. It is thus difficult to give a reliable estimation of the systematic uncertainty of the perturbative series as the latter is far from the asymptotic

TABLE VI. The first three columns contain the results from fitting the entropy density s/T^3 to a polynomial in the coupling $\hat{g}$ according to Eq. (23). Values with errors are the fit parameters, while the other coefficients are set either to zero or to their perturbative value obtained from Ref. [38] (see main text for the details). In the first row, colors refer to Fig. 5. The last column contains the coefficients for the pressure p/T^4, parametrized as in Eq. (24).

k	s_k (orange fit)	s_k (green fit)	s_k (blue fit)	p_k
0	2.969	2.969	2.969	2.969
1	0	0	0	0
2	−5.1(9)	−8.438	−8.438	−8.438
3	5(5)	55.11	55.11	55.11
4	0	$-40.28 + 101.2 \ln \hat{g}^2$	$-40.28 + 101.2 \ln \hat{g}^2$	$-49.77 + 101.2 \ln \hat{g}^2$
5	0	−1174	−1174	−1081
6	0	$4791 - 1629 \ln \hat{g}^2 - 5.1(1.7) \times 10^3$	$4791 - 1629 \ln \hat{g}^2 - 4.0(1.1) \times 10^3$	$4776 - 1401 \ln \hat{g}^2 - 4.0(1.1) \times 10^3$
7	0	$1.3(7) \times 10^4$	$0.7(4) \times 10^4$	$0.4(4) \times 10^4$

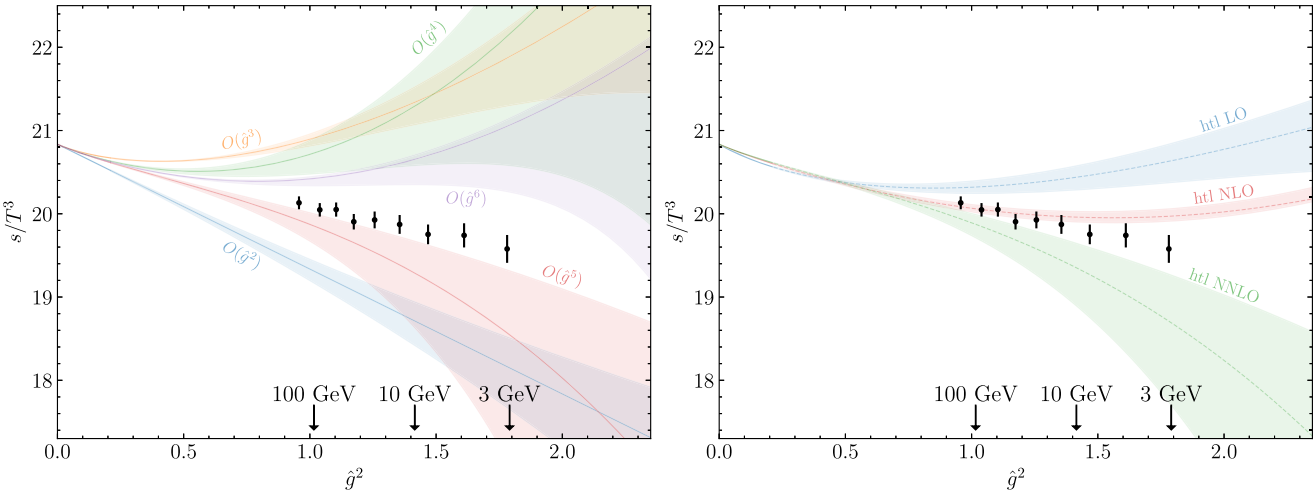

FIG. 6. Black dots are the nonperturbative values of s/T^3 plotted against $\hat{g}^2$. Some values of the physical temperature are reported for reference. In the left plot, the curves represent the predictions of perturbation theory obtained from Ref. [38], each including up to the order in $\hat{g}$ indicated by the label. In the right plot, the curves represent the hard thermal loop perturbation theory [52–54] at leading order, NLO, and NNLO. In both plots, error bands are obtained by a variation of the renormalization scale $\mu = 2\pi T$ by the factors 0.5 and 2.

regime in the temperature range covered by our nonperturbative data (black points in Fig. 6).

Similar conclusions can be drawn by considering the hard thermal loop (htl) resummation of the perturbative expansion [54], see also Ref. [55] for recent developments. The right panel of Fig. 6 compares our nonperturbative results for s/T^3 with the htl curves up to next-to-next-to leading order (NNLO). Again, the shadowed bands correspond to a variation of the renormalization scale $\mu = 2\pi T$ by the factors 0.5 and 2, and the contribution to the bands width from the statistical uncertainty of $\Lambda_{\overline{\mathrm{MS}}}$ is negligible. Even though the expansion appears to converge better in the asymptotically high temperature regime compared to standard perturbation theory, the NLO and NNLO curves are still in tension in the interval of temperature covered by our data, with a discrepancy from a few combined standard deviations at $T \sim 3$ GeV down to about 1 combined standard deviation at $T \sim 165$ GeV. The agreement between the NNLO prediction with the nonperturbative points is at the level of ~1.5 standard deviations if we combine the statistical error of the points with the systematic one due to the renormalization scale variation.

C. Pressure and energy density

Given the parametrization for the entropy density (see the third column of Table VI), we can derive the

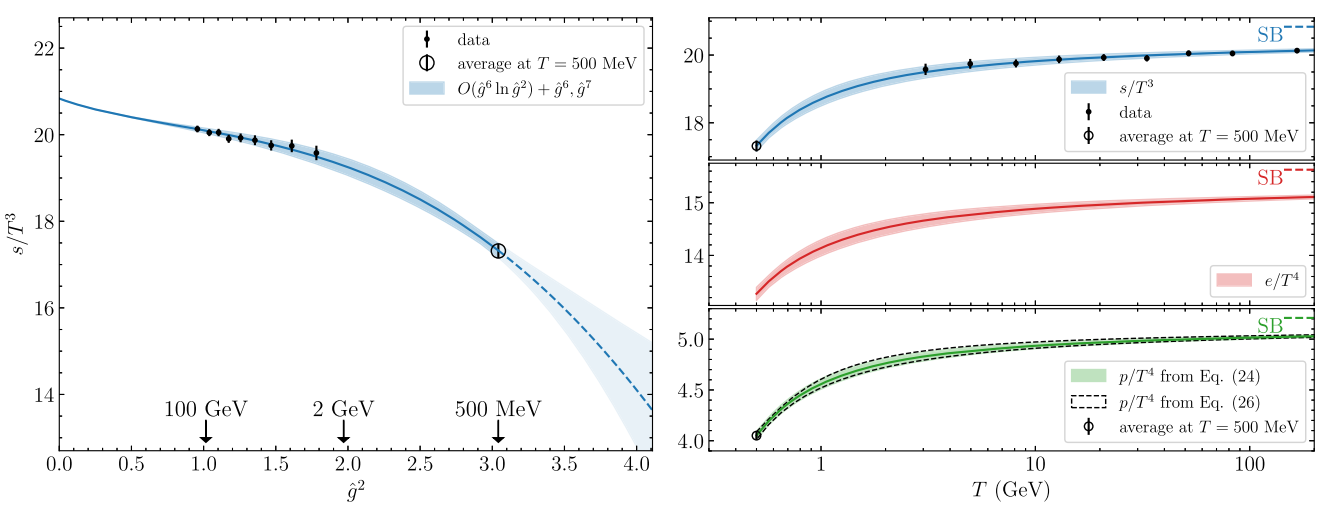

FIG. 7. Left: Normalized entropy density s/T^3 in the continuum limit as a function of $\hat{g}^2$. The blue band is the best parametrization for $T \geq 500$ MeV, and includes the point at $T = 500$ MeV obtained from Refs. [32,49,50] (open circle marker). Right: EOS as a function of the temperature for $T \geq 500$ MeV.

temperature dependence of the pressure $p(T)$ and of the energy density $e(T)$. Following Ref. [38], we parametrize the pressure analogously to the entropy in Eq. (23),

$$\frac{p}{T^4} = \frac{8\pi^2}{45}\sum_k p_k \left(\frac{\hat{g}}{2\pi}\right)^k, \tag{24}$$

where the coefficients $p_0, \ldots, p_6$ are given in Table VI. The coefficient p_7 can be matched to s_7 through the relation $s(T) = \frac{d}{dT}p(T)$, leading to

$$p_7 = s_7 + \frac{45}{16}p_5 + 3p_3. \tag{25}$$

Finally, the energy density is determined using the relation $e = Ts - p$. The three quantities are shown as functions of the temperature in the right panel of Fig. 7, for $T \geq 500$ MeV.

As a check for this result we also determined the pressure by integrating the entropy density with respect to the temperature,

$$p(T) = p(500\ \text{MeV}) + \int_{500\ \text{MeV}}^{T} dT' s(T'), \tag{26}$$

where $p/T^4 = 4.050(38)$ at $T = 500$ MeV is the weighted average of the results for the pressure computed in Refs. [32,49,50]. The comparison of the pressure as a function of the temperature computed following the two strategies described above can be found in the right panel of Fig. 7. The two determinations are perfectly compatible in the entire temperature range.

VII. CONCLUSIONS

We have presented a comprehensive strategy for the nonperturbative study of QCD thermodynamics at very high temperatures. The central ingredients are the definition of lines of constant physics through the running of a renormalized finite-volume coupling across a broad range of energies and the use of shifted boundary conditions to access directly the entropy density. The combination of these elements allowed us to overcome the limitations of traditional lattice methods, such as the need of zero-temperature subtractions and the difficulty of matching bare parameters across widely separated energy scales, like high temperatures and the hadronic scale.

While the main physical results of this work were previously reported in Ref. [5], the present paper provides the full computational framework and numerical validation that support those findings. We have described in detail how these ideas are implemented in practice; the integration techniques in the bare quark mass and in the gauge coupling, the perturbative improvement of lattice observables, the continuum extrapolation strategy and the dedicated checks of systematic effects. Together, these methodological advances provide a framework that is efficient and robust to investigate the thermal features of QCD at high temperatures.

Although the present study has focused on the case of three massless flavors, the techniques developed here are of broader scope. Our simulations span nine temperatures between 3 and 165 GeV, with multiple lattice spacings at each temperature to enable a reliable continuum extrapolation. The entropy density is computed directly from the derivative of the free-energy density with respect to the shift parameter, and the pressure and the energy density are obtained via standard thermodynamic relations. The final results for the EOS are accurate within 1% or better across the entire temperature range, with uncertainties dominated by statistical fluctuations.

A detailed analysis of discretization effects, of finite volume corrections and of topological contributions confirms the robustness of our results. We have also performed a comparison with perturbative predictions, including both standard and hard thermal loop resummations. Our findings show that, at our level of accuracy, higher-order contributions in $\hat{g}^2$ beyond those known, including nonperturbative ones due to ultrasoft modes, are relevant even at temperatures as high as 165 GeV. Furthermore, our results are consistent with existing lattice data at lower temperatures, down to 500 MeV, and a smooth interpolation can be drawn across the entire range.

The methodology discussed in this paper is broadly applicable and can be extended to QCD with four or five massive quark flavors. By disentangling the methodological framework from its first physical application, this work complements earlier results and sets the stage for a systematic program of nonperturbative studies of QCD in the high-temperature regime, with potential impact on cosmology, heavy-ion phenomenology, and the theoretical development of thermal field theory. In particular, the knowledge of the derivative of the free-energy in the shift paves the way to the nonperturbative definition of the QCD energy-momentum tensor, following the strategy proposed in Ref. [10]. Solving this long standing theoretical problem [56–59] would enable further first-principles investigations of the thermal properties of QCD through correlation functions of the energy-momentum tensor.

ACKNOWLEDGMENTS

We acknowledge PRACE for awarding us access to the HPC system MareNostrum4 at the Barcelona Supercomputing Center (Proposals No. 2018194651 and No. 2021240051) where some of the numerical results presented in this paper have been obtained. We also thank CINECA for providing us with a very generous access to Leonardo during the early phases of operations of the machine and for the computer time allocated via the CINECA-INFN, CINECA-Bicocca agreements. The R&D has been carried out on the PC clusters Wilson and Knuth at Milano-Bicocca. We thank all these institutions for the

technical support. This work is (partially) supported by ICSC—Centro Nazionale di Ricerca in High Performance Computing, Big Data and Quantum Computing, funded by European Union—NextGenerationEU.

DATA AVAILABILITY

The data that support the findings of this article are not publicly available upon publication because it is not technically feasible and/or the cost of preparing, depositing, and hosting the data would be prohibitive within the terms of this research project. The data are available from the authors upon reasonable request.

APPENDIX A: LATTICE QCD ACTION

The lattice QCD action, $S_{\rm QCD} = S_G + S_F$, is decomposed in the pure gauge part S_G and in the fermionic one S_F. For the former we employ the Wilson plaquette action [11],

$$S_G = \frac{6}{g_0^2}\sum_x \sum_{\mu<\nu}\left[1 - \frac{1}{3}\mathrm{Re\,tr}\{U_{\mu\nu}(x)\}\right], \tag{A1}$$

where g_0 is the bare coupling, $U_{\mu\nu}$ are the plaquette fields,

$$U_{\mu\nu}(x) = U_\mu(x)U_\nu(x+a\hat{\mu})U_\mu(x+a\hat{\nu})^\dagger U_\nu(x)^\dagger, \tag{A2}$$

$\hat{\mu}, \hat{\nu}$ are unit vectors oriented along the directions μ, ν respectively, and $U_\mu(x) \in \mathrm{SU}(3)$ are the link fields. The fermionic action is

$$S_F = a^4 \sum_x \bar{\psi}(x)(D + M_0)\psi(x), \tag{A3}$$

where the fermionic (antifermionic) fields $\psi(\bar{\psi})$ are triplets in color and flavor space, $M_0 = m_0 \mathbb{1}$ is the bare mass matrix of $N_f = 3$ degenerate quarks, and D is the lattice Dirac operator for which we consider the $O(a)$-improved definition [12,13],

$$D = D_{\rm w} + aD_{\rm sw}. \tag{A4}$$

The operator $D_{\rm w}$ is the massless Wilson-Dirac operator,

$$D_{\rm w} = \frac{1}{2}\{\gamma_\mu(\nabla_\mu^* + \nabla_\mu) - a\nabla_\mu^*\nabla_\mu\}, \tag{A5}$$

where ∇_μ^*, ∇_μ are the covariant lattice derivatives that act on the quark fields as follows:

$$\begin{aligned} a\nabla_\mu\psi(x) &= U_\mu(x)\psi(x+a\hat{\mu}) - \psi(x), \\ a\nabla_\mu^*\psi(x) &= \psi(x) - U_\mu(x-a\hat{\mu})^\dagger\psi(x-a\hat{\mu}). \end{aligned} \tag{A6}$$

The Sheikholeslami-Wohlert term is

$$D_{\rm sw}\psi(x) = c_{\rm sw}(g_0)\frac{1}{4}\sigma_{\mu\nu}\hat{F}_{\mu\nu}(x)\psi(x), \tag{A7}$$

where $\sigma_{\mu\nu} = \frac{i}{2}[\gamma_\mu, \gamma_\nu]$. The field $\hat{F}_{\mu\nu}(x)$ is the clover discretization of the field strength tensor given by

$$\hat{F}_{\mu\nu}(x) = \frac{i}{8a^2}\{Q_{\mu\nu}(x) - Q_{\nu\mu}(x)\} \tag{A8}$$

with

$$\begin{aligned} Q_{\mu\nu}(x) = {} & U_\mu(x)U_\nu(x+a\hat{\mu})U_\mu(x+a\hat{\nu})^\dagger U_\nu(x)^\dagger \\ & + U_\nu(x)U_\mu(x-a\hat{\mu}+a\hat{\nu})^\dagger U_\nu(x-a\hat{\mu})^\dagger U_\mu(x-a\hat{\mu}) \\ & + U_\mu(x-a\hat{\mu})^\dagger U_\nu(x-a\hat{\mu}-a\hat{\nu})^\dagger U_\mu(x-a\hat{\mu}-a\hat{\nu})U_\nu(x-a\hat{\nu}) \\ & + U_\nu(x-a\hat{\nu})^\dagger U_\mu(x-a\hat{\nu})U_\nu(x+a\hat{\mu}-a\hat{\nu})U_\mu(x)^\dagger. \end{aligned} \tag{A9}$$

The coefficient $c_{\rm sw}(g_0)$ has been tuned nonperturbatively [60] so that the spectrum of the theory is free from $O(a)$-discretization effects [13,61].

APPENDIX B: FREE-ENERGY DENSITY IN LATTICE PERTURBATION THEORY

In this appendix we discuss the results of the free-energy density at one-loop order in lattice perturbation theory, evaluated in the infinite spatial volume limit. These expressions, taken from Ref. [10] (in particular Appendixes E and F), are used for the perturbative improvement of the entropy density computed nonperturbatively on the lattice.

1. Preliminaries

In this section we consider lattice QCD with a generic number N_c of colors, and N_f flavors of mass-degenerate $O(a)$-improved Wilson fermions (in the final numerical results we will then set $N_c = 3$, $N_f = 3$). The lattice has compact size L_0 and spatial sizes L_1, L_2, L_3.

In the presence of shifted boundary conditions, the bosonic and the fermionic momenta in the first Brillouin zone are, respectively, given by

$$p_0 = \frac{2\pi n_0}{L_0} - \sum_{k=1}^{3} p_k \xi_k, \qquad p_k = \frac{2\pi n_k}{L_k} \tag{B1}$$

and

$$p_0 = \frac{2\pi n_0}{L_0} + \frac{\pi}{L_0} - \sum_{k=1}^{3} p_k \xi_k, \qquad p_k = \frac{2\pi n_k}{L_k}, \tag{B2}$$

where $n_\mu = 0, 1, \ldots, L_\mu/a - 1$. In momentum space, the free gluonic propagator in the Feynman gauge reads

$$D^{ab}_{\mu\nu}(p) = \frac{\delta_{ab}\delta_{\mu\nu}}{D_G(p)}, \qquad D_G(p) = \sum_{\mu=0}^{3} \hat{p}_\mu^2, \tag{B3}$$

with $\hat{p}_\mu = \frac{2}{a}\sin(\frac{ap_\mu}{2})$, while the free fermionic propagator is

$$S(p) = \frac{-i\gamma_\mu \bar{p}_\mu + m_0(p)}{D_F(p)}, \qquad D_F(p) = \sum_{\mu=0}^{3} \bar{p}_\mu^2 + m_0^2(p), \tag{B4}$$

where $\bar{p}_\mu = \frac{1}{a}\sin(ap_\mu)$, and

$$m_0(p) = m_0 + \frac{a}{2}\sum_{\mu=0}^{3} \hat{p}_\mu^2. \tag{B5}$$

We use the notation $\int_{p_\xi}$ for the integral[3] over the momenta of a generic function $f(p)$,

$$\int_{p_\xi} f(p) = \frac{1}{L_0 L_1 L_2 L_3} \sum_n f(p), \tag{B6}$$

without distinguishing between the bosonic and the fermionic cases since any potential ambiguity is resolved by the propagator that always appears in the integrand. In the infinite spatial volume limit, the integral in Eq. (B6) becomes

$$\int_{p_\xi} f(p) \overset{L_k\to\infty}{\to} \frac{1}{L_0}\sum_{n_0} \int_{BZ} \frac{d^3\boldsymbol{p}}{(2\pi)^3} f(p), \tag{B7}$$

where BZ stands for the Brillouin zone.

a. Some relevant integrals

We define here some integrals that appear in the lattice perturbative expansions,

$$B^{(0)} = \int_{p_\xi} \frac{1}{D_G(p)}, \tag{B8}$$

$$B^{(3)}_\mu = \int_{p_\xi} \frac{\mathrm{c}_\mu(p)}{D_G(p)}, \tag{B9}$$

$$F^{(4)}_{\mu\nu} = \int_{p_\xi} \frac{\bar{p}_\mu \mathrm{c}_\nu(p)}{D_F(p)}, \tag{B10}$$

$$F^{(5)}_\mu = \int_{p_\xi} \frac{m_0(p)\bar{p}_\mu}{D_F(p)}, \tag{B11}$$

$$F^{(6)}_{\mu\nu} = \int_{p_\xi} \frac{m_0(p)\bar{p}_\mu \mathrm{c}_\nu(p)}{D_F^2(p)}, \tag{B12}$$

$$F^{(7)}_\mu = \int_{p_\xi} \frac{m_0^2(p)\bar{p}_\mu}{D_F^2(p)}, \tag{B13}$$

$$F^{(8)} = \int_{p_\xi} \frac{m_0(p)}{D_F(p)}, \tag{B14}$$

where $\mathrm{c}_\mu(p) = \cos(ap_\mu)$.

b. Critical mass at one-loop order

In perturbation theory we define the critical mass m_{cr} with the same prescription[4] followed nonperturbatively, as the value of bare quark mass for which the PCAC mass vanishes in the Schrödinger functional setup [62,63]. At one-loop order,

$$\begin{aligned} am_{\mathrm{cr}} &= am_{\mathrm{cr}}^{(0)} + \delta am_{\mathrm{cr}}^{(0)} \\ &\quad + g_0^2(am_{\mathrm{cr}}^{(1)} + \delta am_{\mathrm{cr}}^{(1,0)} + N_f \delta am_{\mathrm{cr}}^{(1,1)}), \end{aligned} \tag{B15}$$

where $am_{\mathrm{cr}}^{(0)} = 0$, and we define

$$am_{\mathrm{cr}}^{(1)} = \frac{N_c^2 - 1}{N_c} am_{\mathrm{cr}}^{(1,N_c)}, \tag{B16}$$

$$\delta am_{\mathrm{cr}}^{(1,0)} = \frac{N_c^2 - 1}{N_c} \delta am_{\mathrm{cr}}^{(1,N_c,0)}, \tag{B17}$$

$$\delta am_{\mathrm{cr}}^{(1,1)} = \frac{N_c^2 - 1}{N_c} \delta am_{\mathrm{cr}}^{(1,N_c,1)}, \tag{B18}$$

with [63]

$$\begin{aligned} am_{\mathrm{cr}}^{(1,N_c)} &= -0.16285705871085(1) \\ &\quad + c_{\mathrm{sw}} 0.04348303388205(10) \\ &\quad + c_{\mathrm{sw}}^2 0.01809576878142(1). \end{aligned} \tag{B19}$$

[3]Strictly speaking, the quantity in Eq. (B6) is a sum over the discrete momentum components. In the following we call these sums integrals because we are interested in the thermodynamic limit, where the sum becomes a sum of integrals over the spatial momenta.

[4]This is alternative to the definition based on the quark self-energy, and the two differ by lattice artifacts.

At this order, the improvement coefficient $c_{\rm sw}$ is either 0 or 1 for the unimproved or improved theory, respectively. The quantities $\delta am_{\rm cr}^{(0)}$, $\delta am_{\rm cr}^{(1,0)}$, $\delta am_{\rm cr}^{(1,1)}$ are the cutoff effects in the perturbative determination of the critical mass. The values for $\delta am_{\rm cr}^{(0)}$, $am_{\rm cr}^{(1)} + \delta am_{\rm cr}^{(1,0)}$ and $\delta am_{\rm cr}^{(1,1)}$ for $N_c = N_f = 3$ and $c_{\rm sw} = 1$ can be found in Table 7.1 of Ref. [62]. In our perturbative calculations at one-loop order, the proper chiral limit is thus obtained by setting in the integrals the bare quark mass to the tree-level value of Eq. (B15).

2. Free-energy density

We collect here the expression of the free-energy density in lattice perturbation theory at one-loop order. Results are taken from Appendix F of Ref. [10]. At given L_0/a, we write the perturbative expansion as

$$f_{\boldsymbol{\xi}} = f^{(0)} + g_0^2 f^{(1)}, \tag{B20}$$

where, for simplicity, we omit the dependence on L_0/a and suppress the dependence of the perturbative coefficients on the shift $\boldsymbol{\xi}$. The tree-level coefficient reads

$$f^{(0)} = (N_c^2 - 1) f^{G(0)} + N_c N_f f^{F(0)} \tag{B21}$$

with

$$f^{G(0)} = \int_{p_\xi} \ln\,[a^2 D_G(p)], \tag{B22}$$

$$f^{F(0)} = -2 \int_{p_\xi} \ln\,[a^2 D_F(p)]. \tag{B23}$$

At one-loop order we have

$$\begin{aligned} f^{(1)} = (N_c^2 - 1)\Bigg\{ & N_c f^{G(1,N_c)} + \frac{1}{N_c} f^{G(1,\frac{1}{N_c})} \\ & + N_f \Bigg[f^{F(1,N_f)} + \mathcal{F}^{F1} + \mathcal{F}^{F2} + \frac{\partial f^{F(0)}}{\partial am_0} \\ & \times \left(am_{\rm cr}{}^{(1,N_c)} + \delta am_{\rm cr}{}^{(1,N_c,0)} + N_f \delta am_{\rm cr}{}^{(1,N_c,1)} \right) \Bigg] \Bigg\}. \end{aligned} \tag{B24}$$

The gluonic coefficients are given by

$$\begin{aligned} f^{G(1,N_c)} = \Bigg\{ & (B^{(0)})^2 - \frac{1}{2} \sum_\sigma [B^{(0)} - B_\sigma^{(3)}]^2 + \frac{1}{2} a^2 K_1 \\ & + \frac{1}{24} a^4 K_2 - \frac{1}{2a^2} B^{(0)} \Bigg\}, \end{aligned} \tag{B25}$$

$$f^{G(1,\frac{1}{N_c})} = \frac{1}{2} \left\{ \sum_\sigma [B^{(0)} - B_\sigma^{(3)}]^2 + \frac{1}{8a^4} \right\}, \tag{B26}$$

where we defined the integrals

$$K_1 = \int_{p_\xi;q_\xi;k_\xi} \frac{\bar\delta(p+q+k)}{D_G(p) D_G(q) D_G(k)} \sum_\mu \hat p_\mu^2 \hat q_\mu^2, \tag{B27}$$

$$K_2 = \int_{p_\xi;q_\xi;k_\xi} \frac{\bar\delta(p+q+k)}{D_G(p) D_G(q) D_G(k)} \sum_\mu \hat p_\mu^2 \hat q_\mu^2 \hat k_\mu^2, \tag{B28}$$

with $\bar\delta(p) = a^4 \sum_x e^{ipx}$. The fermionic part is

$$\begin{aligned} f^{F(1,N_f)} = {} & B^{(0)} \left[\frac{1}{a^2} - a(am_0 + 4) F^{(8)} \right] \\ & + \int_{q_\xi;p_\xi;k_\xi} \frac{\bar\delta(p-q-k)}{D_G(q) D_F(p) D_F(k)} \\ & \times \Bigg[am_0(k) \sum_\sigma \bar r_\sigma \bar p_\sigma + am_0(p) \sum_\sigma \bar k_\sigma \bar r_\sigma \\ & - m_0(k) m_0(p) \sum_\sigma \mathrm{c}_\sigma(r) + \sum_\sigma \bar p_\sigma \bar k_\sigma (\mathrm{c}_\sigma(r) - 3) \Bigg], \end{aligned} \tag{B29}$$

where $r = p + k$. The terms $\mathcal{F}^{F1}$ and $\mathcal{F}^{F2}$ are the contributions from the $O(a)$ improvement in the Wilson action,

$$\begin{aligned} \mathcal{F}^{F1} = {} & -\frac{a c_{\rm sw}}{2} \int_{q_\xi;p_\xi;k_\xi} \frac{\bar\delta(p-q-k)}{D_G(q) D_F(p) D_F(k)} \\ & \times \Bigg\{ a \sum_{\sigma\rho} [(\bar p_\rho + \bar k_\rho) \bar q_\sigma (\bar p_\sigma \bar k_\rho - \bar k_\sigma \bar p_\rho)] \\ & - \sum_\sigma \Bigg\{ \bar q_\sigma [m_0(k) \bar p_\sigma \\ & - m_0(p) \bar k_\sigma] \sum_{\rho \neq \sigma} [\mathrm{c}_\rho(p) + \mathrm{c}_\rho(k)] \Bigg\} \Bigg\}, \end{aligned} \tag{B30}$$

$$\begin{aligned} \mathcal{F}^{F2} = {} & \frac{a^2 c_{\rm sw}^2}{8} \int_{q_\xi;p_\xi;k_\xi} \frac{\bar\delta(p-q-k)}{D_G(q) D_F(p) D_F(k)} \\ & \times \Bigg\{ m_0(p) m_0(k) \sum_\sigma \Bigg\{ \bar q_\sigma^2 \Bigg[3 + \sum_{\rho \neq \sigma} \mathrm{c}_\rho(q) \Bigg] \Bigg\} \\ & + 2 \sum_{\sigma\rho} \bar k_\sigma \bar q_\sigma \bar p_\rho \bar q_\rho \left(2 - \mathrm{c}_\sigma(q) + \sum_{\lambda \neq \rho} \mathrm{c}_\lambda(q) \right) \\ & - \sum_{\sigma\rho} \bar k_\sigma \bar p_\sigma \bar q_\rho^2 \left(1 - 2\mathrm{c}_\sigma(q) + \sum_{\lambda \neq \rho} \mathrm{c}_\lambda(q) \right) \Bigg\}. \end{aligned} \tag{B31}$$

The last term in Eq. (B24) comes from the one-loop order correction to the critical mass $am_{\rm cr}$, with a coefficient given by the derivative in the bare mass of the tree-level fermionic free energy,

$$\frac{\partial f^{F(0)}}{\partial m_0} = -4 F^{(8)}. \tag{B32}$$

3. Infinite volume limit of gluonic contributions

To evaluate the lattice sums that appear in the computation of the perturbative coefficients in finite volume, we have regularized the gluonic propagator by removing the zero mode occurring when the momentum of the gluon vanishes. The finite size effects of quantities containing gluonic loops are then powerlike in the inverse spatial size of the box; we set $L_1 = L_2 = L_3 = L$—with leading scaling of $O(1/L)$ or $O(1/L^3)$ as $L \to \infty$. The $O(1/L)$ effects can be removed analytically, while the $O(1/L^3)$ ones can be extrapolated numerically with high accuracy to the thermodynamic limit where any systematic effects introduced by the gluon zero-mode subtraction disappear. The lattice sums required for the integrals at one-loop order have been performed in coordinate space [64] after using a efficient Fast Fourier Transform algorithm for the computation of the propagators. We ran in quadruple precision because of large cancellations occurring in the lattice sums appearing in the various terms.

a. Tree-level integrals

The infinite spatial volume limit of the integrals $B^{(0)}$, $B^{(3)}_\mu$, and $f^{G(0)}$ is obtained by replacing the discrete sums over p_1, p_2, p_3 with continuum integrations according to Eq. (B7). If the shift is chosen in the first spatial direction, the integration in p_2 and p_3 can be done analytically [64] and we obtain the following expressions:

$$B^{(0)}_\infty = \frac{1}{2L_0}\sum_{n_0}\int_0^\infty dx \int_{BZ}\frac{dp_1}{2\pi} I_0(x)^2 e^{xC(p_0,p_1)}, \tag{B33}$$

$$B^{(3)}_{\mu,\infty} = \frac{1}{2L_0}\sum_{n_0}\int_0^\infty dx \int_{BZ}\frac{dp_1}{2\pi} I_0(x)^2 \mathrm{c}_\mu(p) e^{xC(p_0,p_1)}, \tag{B34}$$

for $\mu = 0, 1$, while for $k = 2, 3$ we have

$$B^{(3)}_{k,\infty} = \frac{1}{2L_0}\sum_{n_0}\int_0^\infty dx \int_{BZ}\frac{dp_1}{2\pi} I_0(x) I_1(x) e^{xC(p_0,p_1)}, \tag{B35}$$

and finally

$$f^{G(0)}_\infty = \frac{1}{a^2 L_0}\sum_{n_0}\int_{BZ}\frac{dp_1}{2\pi}\left\{\ln\left[4 - 2C(p_0,p_1)\right] + \int_0^\infty dx \frac{[e^{-2x} - I_0(x)^2]}{x} e^{xC(p_0,p_1)}\right\}. \tag{B36}$$

In these equations $C(p_0, p_1) = \mathrm{c}_0(p) + \mathrm{c}_1(p) - 4$ and I_0 and I_1 are the modified Bessel functions of the first kind [65]. The integrals over p_1 and x can then be easily computed numerically with high accuracy.

b. Integrals at one-loop order

We discuss here the computation of the integrals K_1, K_2 in the thermodynamic limit. These integrals, defined in Eqs. (B27) and (B28), enter in the one-loop order gluonic contribution $f^{G(1,N_c)}$ of Eq. (B25). The integral K_1 has leading finite volume effects of order $O(1/L)$. In the small momentum limit of k, the $\bar{\delta}$ function leads to $q \sim -p$ and we have the effective behavior,

$$K_1 \sim \int_{k_\xi}\frac{1}{D_G(k)}\int_{p_\xi}\frac{\sum_\mu \hat{p}^4_\mu}{D^2_G(p)} = B^{(0)} c_{K_1}, \tag{B37}$$

whose leading $O(1/L)$ finite size effects are given by $B^{(0)}$. The second integral in rhs, denoted by c_{K_1}, is the residual at the pole $k = 0$ of the integrand function of K_1. It is now convenient to consider the subtracted integral

$$K'_1 = K_1 + c_{K_1}(B^{(0)}_\infty - B^{(0)}), \tag{B38}$$

which attains the same value of K_1 in the thermodynamic limit but with the faster convergence rate $O(1/L^3)$, as the leading $O(1/L)$ finite volume corrections of K_1 have been removed. Moreover, the integral appearing in the coefficient c_{K_1} can be easily computed with high accuracy.

In left panel of Fig. 8 we compare the approach to the thermodynamic limit of K'_1 (orange square markers) and K_1 (blue circle markers). The system size in the spatial directions increases from $L/a = 96$ up to $L/a = 288$. For all practical purposes we can quote as the infinite volume limit the value of K'_1 at the largest volume, whose discrepancy with respect to the extrapolation is well below the permille level.

The leading finite size corrections of the integral K_2 are of order $O(1/L^3)$ and they are negligible at the largest size $L/a = 288$ that we have considered. Thus, we take that value as the thermodynamic limit.

4. Infinite volume limit of fermionic contributions

We have extrapolated to the thermodynamic limit the tree-level fermionic free-energy density $f^{F(0)}$, Eq. (B23), and the one-loop order mass counterterm, Eq. (B32), by increasing L/a from 96 to 288 at fixed L_0/a. The convergence to the infinite volume limit is very fast because, at asymptotically high temperatures, fermions develop a thermal mass $M_{\mathrm{th}} \sim \pi T$ and finite volume effects are exponentially suppressed as $e^{-M_{\mathrm{th}}L}$ [9]. At the largest volume, finite size effects are well below the permille level, and in practice the results can be considered as the values in the thermodynamic limit.

The fermionic contributions at one-loop order have powerlike finite size effects in $1/L$ because of integrable singularities related to virtual gluons in the loops. For example, in the fermionic coefficient $f^{F(1,N_f)}$ of Eq. (B29), we have the integral,

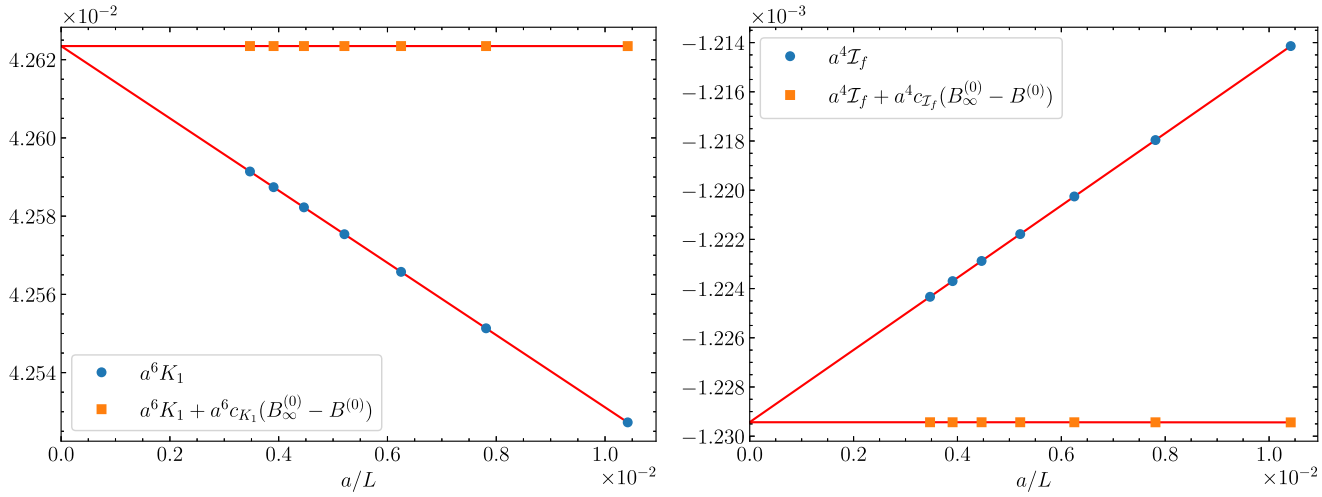

FIG. 8. Volume dependence of the integrals K_1 and $\mathcal{I}_f$ respectively defined in Eqs. (B27) and (B39), for the representative case $L_0/a = 6$ and shift $L_0\boldsymbol{\xi} = (8a, 0, 0)$. The spatial size L/a of the lattice ranges between 96 and 288. For both integrals the comparison with the subtracted definition is shown, see main text for the details. Red lines represent the extrapolations to the thermodynamic limit.

$$\mathcal{I}_f \equiv \int_{q_\xi;p_\xi;k_\xi} \frac{\bar{\delta}(p-q-k)}{D_G(q)D_F(p)D_F(k)} \Big[am_0(k)\sum_\sigma \bar{r}_\sigma \bar{p}_\sigma + am_0(p)\sum_\sigma \bar{k}_\sigma \bar{r}_\sigma - m_0(k)m_0(p)\sum_\sigma \mathrm{c}_\sigma(r) + \sum_\sigma \bar{p}_\sigma \bar{k}_\sigma(\mathrm{c}_\sigma(r) - 3)\Big], \tag{B39}$$

whose integrand has a pole when the gluonic momentum vanishes $q \to 0$ and $p \sim k$. Following the same strategy as for the computation of K_1 in the previous section, we have introduced the subtracted integral,

$$\mathcal{I}'_f = \mathcal{I}_f + c_{\mathcal{I}_f}(B_\infty^{(0)} - B^{(0)}), \tag{B40}$$

where $c_{\mathcal{I}_f}$ is the residual at the pole $q = 0$ of the integrand function of $\mathcal{I}_f$,

$$c_{\mathcal{I}_f} = \int_{p_\xi} \frac{1}{D_F^2(p)} \Big[2am_0(p)\sum_\sigma \overline{(2p)}_\sigma \bar{p}_\sigma - m_0^2(p)\sum_\sigma \mathrm{c}_\sigma(2p) + \sum_\sigma \bar{p}_\sigma^2(\mathrm{c}_\sigma(2p) - 3)\Big], \tag{B41}$$

and can be easily computed numerically with high accuracy. The integrals $\mathcal{I}'_f$ and $\mathcal{I}_f$ have the same thermodynamic limit, but the leading finite volume effects of the former are of $O(1/L^3)$ as the leading ones of the latter, of $O(1/L)$, have been subtracted. The data for $\mathcal{I}'_f$ are represented in the right panel of Fig. 8 (orange square markers) in comparison with the results for $\mathcal{I}_f$ (blue circle markers). As before, the residual finite size effects after the subtraction are negligible and we can take the value at the largest size $L/a = 288$ as the thermodynamic limit.

The same holds for the infinite volume extrapolation of the integrals $\mathcal{F}^{F1}$, $\mathcal{F}^{F2}$ defined respectively in Eqs. (B30) and (B31), whose finite size corrections are already of $O(1/L^3)$.

APPENDIX C: CHOICE OF THE SHIFT PARAMETER

In this appendix we discuss the choice of the shift parameter $\boldsymbol{\xi}$ that defines the boundary conditions for the gauge and fermionic fields along the compact direction, see Eqs. (1) and (2). To this aim we consider the following generalization of Eq. (6),

$$\frac{s}{T^3} = \frac{(1+\boldsymbol{\xi}^2)^3}{\boldsymbol{\xi}\cdot\boldsymbol{v}} L_0^4 \frac{L_0}{2a}\left(f_{\boldsymbol{\xi}+\frac{a}{L_0}\boldsymbol{v}} - f_{\boldsymbol{\xi}-\frac{a}{L_0}\boldsymbol{v}}\right), \tag{C1}$$

where the spatial vector $\boldsymbol{v}$ defines the direction and the magnitude of the finite difference. In the continuum limit, this finite difference becomes the directional derivative of $f_{\boldsymbol{\xi}}$ along $\boldsymbol{v}$. Different values of $\boldsymbol{\xi}$ and $\boldsymbol{v}$ lead to different discretizations of the entropy density, with different cutoff effects and relative error; a convenient choice should minimize both of them. We have considered the following set of shift vectors:

$$\boldsymbol{\xi} = \{(1/2,0,0),(1,0,0),(1/2,1/2,0),(1,1,0),(2,0,0)\}, \tag{C2}$$

so as to explore the trend of discretization effects and relative error of s/T^3 for increasing norm of $\boldsymbol{\xi}$ and for shifts in one or two directions. For shifts in the first direction only, we have taken $\boldsymbol{v} = (1,0,0)$ [one-point finite difference in Eq. (C1)] or $\boldsymbol{v} = (2,0,0)$ (two-point finite difference). For nonzero shifts in the first and second direction, we have

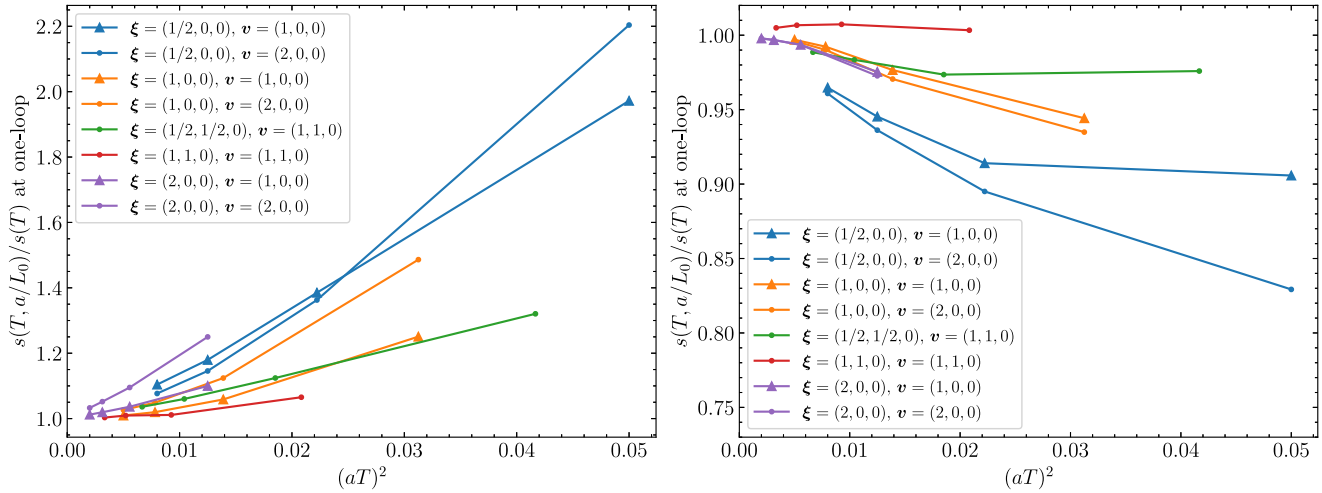

FIG. 9. Left: Results in lattice perturbation theory at one-loop order of s/T^3, normalized to the continuum limit, for some choices of $\boldsymbol{\xi}$ and $\boldsymbol{v}$. In the perturbative expressions we have used the SF coupling $\bar{g}^2_{\mathrm{SF}}(1/L_0)$ at the temperature T_1. The lines connecting the points are drawn to guide the eye. Right: Same as left panel, but with tree-level improved data according to Eq. (18).

considered $\boldsymbol{v} = (1, 1, 0)$ (one-point simultaneous finite difference in both directions).

1. Discretization effects

We have studied how discretization effects depend on the values of $\boldsymbol{\xi}$ and $\boldsymbol{v}$ using lattice perturbation theory at one-loop order. Figure 9 shows the entropy, computed as in Eq. (C1), normalized to the continuum result at one-loop order, for several values of the parameters under investigation. Data with $\boldsymbol{\xi} = (1/2, 0, 0)$ have the largest cutoff effects, data with $\boldsymbol{\xi} = (1, 1, 0)$ have the smallest. Most of the discretization effects can be actually removed with a tree-level improvement as in Eq. (18) (with $g = 0$), and the remaining lattice artifacts are of the order of a few percent for all the considered values of the shift but for $\boldsymbol{\xi} = (1/2, 0, 0)$, which still shows a 10%–15% deviation from the continuum limit at the coarsest point. Furthermore, at a given $\boldsymbol{\xi}$, the tree-level improvement removes almost all the discrepancy between the one-point and two-point discretizations of the finite difference. The validity of these results at the nonperturbative level is confirmed by Fig. 10, where the cutoff effects of the nonperturbative data for $\boldsymbol{\xi} = (1, 0, 0)$, $\boldsymbol{v} = (2, 0, 0)$ compare very well with the perturbative ones at the temperatures T_1 and T_7. Similar conclusions hold at all other temperatures.

This study shows that the discretization effects of s/T^3 can be removed very efficiently through the perturbative

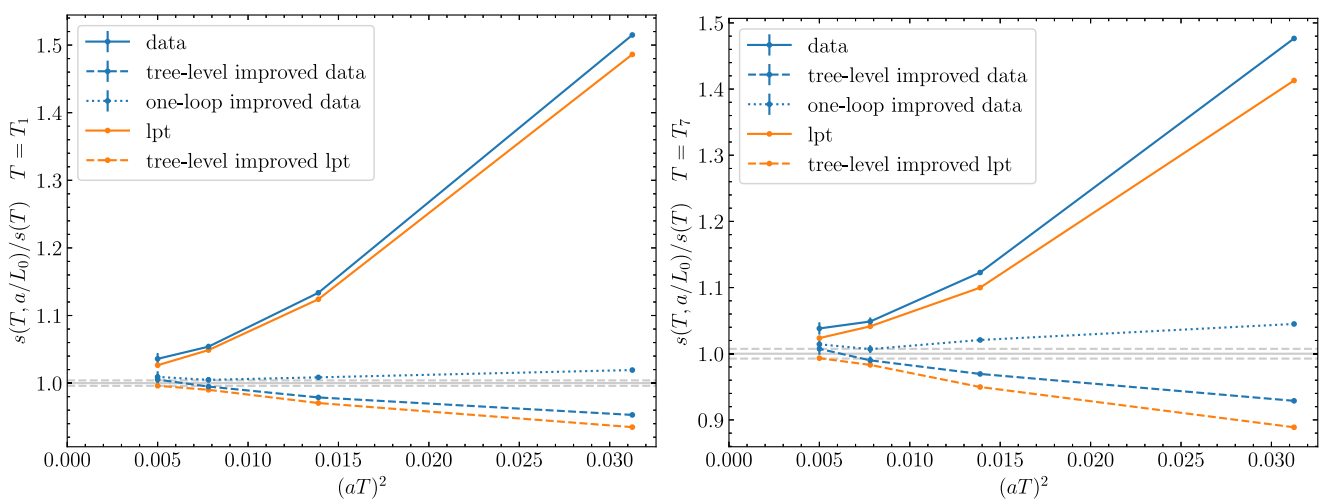

FIG. 10. Nonperturbative results of s/T^3 for $\boldsymbol{\xi} = (1, 0, 0)$ and $\boldsymbol{v} = (2, 0, 0)$, in comparison with lattice perturbation theory (lpt) at one-loop order. Nonperturbative and perturbative results are normalized to their respective continuum limits. The left panel shows data at the temperature T_1, the right panel at the temperature T_7. The gray dashed lines represent the uncertainty of the extrapolated nonperturbative continuum limit. The lines connecting the points are drawn to guide the eye.

improvement, after which all the considered values of $\boldsymbol{\xi}$ and $\boldsymbol{v}$, with the only exception of $\boldsymbol{\xi} = (1/2, 0, 0)$, are comparable in terms of residual lattice artifacts.

2. Relative error

In the presence of shifted boundary conditions, the temperature of the thermal system depends on the shift through the relation $T^{-1} = L_0\sqrt{1+\boldsymbol{\xi}^2}$. At a given L_0, the temperature changes by less than a factor 2 with respect to the reference case $\boldsymbol{\xi} = (1, 0, 0)$ when the shift is varied within the values listed in Eq. (C2). Since the entropy density increases slowly from 3 to 165 GeV (about 3%, see Table V), at these temperatures and at a given L_0 we can assume s/T^3 to be approximately constant when the shift is changed among the values under investigation. Using this assumption in Eq. (C1), we get the scaling,

$$L_0^4\left(f_{\boldsymbol{\xi}+\frac{a}{L_0}\boldsymbol{v}} - f_{\boldsymbol{\xi}-\frac{a}{L_0}\boldsymbol{v}}\right) \propto \frac{\boldsymbol{\xi}\cdot\boldsymbol{v}}{(1+\boldsymbol{\xi}^2)^3}, \tag{C3}$$

for the finite difference of the free-energy, while the related variance is expected to be mostly independent on the shift. This leads to the relation,

$$\frac{\sigma[s]}{s} \propto \frac{(1+\boldsymbol{\xi}^2)^3}{\boldsymbol{\xi}\cdot\boldsymbol{v}}, \tag{C4}$$

for the relative accuracy of the entropy density. A direct nonperturbative check of this scaling would be computationally very demanding. Similarly to Sec. V A, we have instead verified the analogous relation for the energy-momentum tensor,

$$\frac{\sigma[\langle T_{0k}^{R,\{6\}}\rangle_{\boldsymbol{\xi}}]}{\langle T_{0k}^{R,\{6\}}\rangle_{\boldsymbol{\xi}}} \propto \frac{(1+\boldsymbol{\xi}^2)^3}{\xi_k}, \tag{C5}$$

coming from Eq. (16). We have simulated 8×48^3 lattices at the temperature T_1 and at the values of shift given in Eq. (C2). For each ensemble, the measured expectation values of the components $T_{01}^{G,\{6\}}$ and $T_{01}^{F,\{6\}}$, defined in Eq. (17), are reported in Table VII. The data confirm the assumption that the variance is mostly independent on the shift. Furthermore, the relative errors are well described by the expected scaling Eq. (C5).

Given that the assumptions underlying Eq. (C4) are well supported by the nonperturbative results, we have collected in Table VIII the expected scaling for the relative error of s/T^3 at the different choices of $\boldsymbol{\xi}$ and $\boldsymbol{v}$ under investigation. The two-point finite difference leads to halved relative errors with respect to the one-point one. Since any additional discretization effects can be removed efficiently with the tree-level improvement (see Appendix C 1), the choice $\boldsymbol{v} = (2, 0, 0)$ is preferable to $\boldsymbol{v} = (1, 0, 0)$. On the other hand, the relative error increases with the norm of the shift, at the point that the shifts $\boldsymbol{\xi} = (1, 1, 0)$ and $\boldsymbol{\xi} = (2, 0, 0)$ are severely penalized. We may also exclude $\boldsymbol{\xi} = (1/2, 0, 0)$, which leads to larger cutoff effects compared to the other shifts. Choices like $\boldsymbol{\xi} = (1/2, 1/2, 0)$ with $\boldsymbol{v} = (1, 0, 0)$ would lead to twice the relative error of $\boldsymbol{v} = (1, 1, 0)$, and if we choose instead $\boldsymbol{v} = (2, 0, 0)$ the signal is the same as $\boldsymbol{v} = (1, 1, 0)$ while the cutoff effects are expected to be worse. The relevant candidates are thus $\boldsymbol{\xi} = (1, 0, 0)$ with $\boldsymbol{v} = (2, 0, 0)$ or $\boldsymbol{\xi} = (1/2, 1/2, 0)$ with $\boldsymbol{v} = (1, 1, 0)$. After the tree-level improvement, their residual cutoff effects are comparable, while the relative error on the entropy with $\boldsymbol{\xi} = (1/2, 1/2, 0)$ is about 15% less. At present, our simulation code allows only for even values of $L_0\boldsymbol{\xi}$ in every spatial direction. We have therefore chosen $\boldsymbol{\xi} = (1, 0, 0)$ for which all the resolutions $L_0/a = 4, 6, 8, 10$ can be simulated, also considering that lattices with $L_0/a > 10$ are computationally very demanding.

TABLE VII. Results for the energy-momentum tensor from 8×48^3 lattices at the temperature T_1. Each ensemble has 100 measurements. The relative error of the matrix elements is expected to scale as the numbers in the last column.

$\boldsymbol{\xi}$	$L_0^4\langle T_{01}^{G,\{6\}}\rangle_{\boldsymbol{\xi}}$	$L_0^4\langle T_{01}^{F,\{6\}}\rangle_{\boldsymbol{\xi}}$	Eq. (C5)
(1/2, 0, 0)	−1.60(24)	−3.50(8)	3.91
(1, 0, 0)	−0.87(22)	−1.60(9)	8.00
(1/2, 1/2, 0)	−0.92(19)	−1.88(9)	6.75
(1, 1, 0)	−0.18(21)	−0.40(10)	27.00
(2, 0, 0)	−0.17(28)	−0.21(9)	62.50

TABLE VIII. Expected scaling of $\sigma[s]/s$.

$\boldsymbol{\xi}$	$\boldsymbol{v}$	Eq. (C4)
(1/2, 0, 0)	(1, 0, 0)	3.91
(1/2, 0, 0)	(2, 0, 0)	1.95
(1, 0, 0)	(1, 0, 0)	8.00
(1, 0, 0)	(2, 0, 0)	4.00
(1/2, 1/2, 0)	(1, 1, 0)	3.38
(1, 1, 0)	(1, 1, 0)	13.50
(2, 0, 0)	(1, 0, 0)	62.50
(2, 0, 0)	(2, 0, 0)	31.25

APPENDIX D: SYSTEMATICS FROM THE NUMERICAL QUADRATURES

In this appendix we discuss the choice of the integration scheme for the integral in the bare subtracted mass defined in Sec. IV. We have used lattice perturbation theory at tree level as guidance, since at this perturbative order we can calculate both sides of the relation,

$$\frac{\Delta(f_{\boldsymbol{\xi}} - f_{\boldsymbol{\xi}}^{\infty})}{\Delta\xi_k} = -\int_0^\infty dm_q \frac{\Delta\langle\bar{\psi}\psi\rangle_{\boldsymbol{\xi}}^{m_q}}{\Delta\xi_k}, \tag{D1}$$

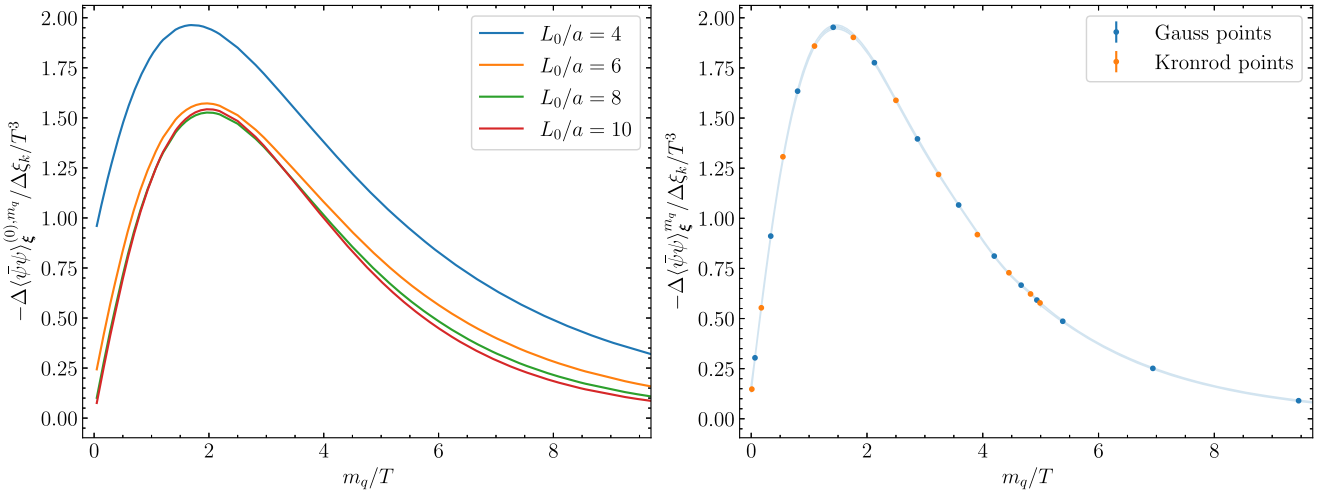

FIG. 11. Left: Discrete derivative of the expectation value of the scalar density with respect to the shift, computed at tree level in lattice perturbation theory at several values of m_q/T. Right: Nonperturbative results at inverse bare coupling $6/g_0^2 = 8.2170$ computed on 6×144^3 lattices.

and thus assess the systematic effects induced by the computation of the integral by means of numerical quadratures.

The left panel of Fig. 11 shows that the integrand function, at tree level in lattice perturbation theory, has a very smooth dependence on the subtracted quark mass m_q/T. The mild peaked shape suggests to split the numerical integration in three intervals for increasing bare mass, such that the first segment is about 80% of the total integral, the second segment about 20% and the last part is at most about equal to the target absolute error of the full integral. A numerical exploration of the problem led to the integration scheme reported in Eq. (14). When the latter is applied to Eq. (D1) at tree level, the resulting systematic effects from the numerical quadratures are at most $1/10$ of the target statistical accuracy. A side advantage of splitting the integration in several domains is that, if needed, the numerical accuracy of each interval can be improved independently from the others by using, for instance, higher order quadratures.

The comparison of the right panel of Fig. 11 with the left panel reveals that the nonperturbative behavior of the integrand function is very similar to its perturbative counterpart. The chosen integration scheme is thus expected to be appropriate also for the nonperturbative case.

We have explicitly checked on the nonperturbative results that the systematic effects from the numerical quadratures are negligible within the statistical error by improving the computation of the integral in the domain $\{0 \le m_q/T \le 5\}$ at the bare parameters $6/g_0^2 = 8.2170$, $L_0/a = 6$ (corresponding to the temperature T_2) using the Gauss-Kronrod quadrature rule. Any systematic effects from the other integration domains are expected to be completely subdominant because the integrand function for $m_q/T \ge 5$ is monotonically decreasing, and because the bulk of the integral comes from the first domain. The n-point Gauss quadrature integrates exactly polynomials up to order $2n - 1$. The Gauss-Kronrod quadrature adds $n + 1$ points to the Gauss quadrature, and integrates exactly polynomials up to order $3n + 1$ [66]. The points of the Gauss quadrature are shown in the right panel of Fig. 11 as blue markers, and the blue shadowed band is a polynomial interpolation of them. We have generated on the lattice the additional 11 points (orange markers) for the $n = 10 + 11$ Gauss-Kronrod rule. The error bars are smaller than the markers, and the orange points are compatible within about 0.5σ with the blue shadowed interpolation.

The comparison between the two numerical integrations is in Table IX, where we give the full result for s/T^3 when the integral in the bare quark mass is computed as in Eq. (14) using either the $n = 10$ Gauss rule or the $n = 10 + 11$ Gauss-Kronrod rule for the domain $\{0 \le m_q/T \le 5\}$. The statistical accuracy of the points have been tuned so that the two results have comparable absolute errors. The tiny difference is several times smaller than one combined standard deviation. Furthermore, the shape of the nonperturbative integrand function depends very mildly on the temperature and on the value of L_0/a. The systematic effects from the Gauss quadratures are thus negligible for all the temperatures and lattice spacings that we have simulated.

TABLE IX. Results for the normalized entropy density at inverse bare coupling squared $6/g_0^2 = 8.2170$ computed on 6×144^3 lattices, using either the Gauss quadrature or the Gauss-Kronrod quadrature. See main text for the details.

Quadrature	s/T^3
Gauss	22.77(5)
Gauss-Kronrod	22.76(5)

APPENDIX E: DETAILS ON THE LATTICE QCD SIMULATIONS

We have simulated lattice QCD with $N_f = 3$ degenerate flavors of quarks by using the HMC algorithm. Our code is based on the package openQCD-1.6 [67,68], modified for including shifted boundary conditions [14,69]. The doublet of up and down quarks have been simulated with an optimized twisted-mass Hasenbusch preconditioning of the quark determinant [70]. The strange quark has been included with the rational hybrid Monte Carlo (RHMC) algorithm [71,72]. We employed even-odd preconditioning for all the three flavors [73]. The solution of the Dirac equation in the molecular dynamics trajectory was performed with a standard conjugate gradient with chronological inversion.

1. Tuning of the HMC

We performed the tuning of the algorithm parameters at the different values of the hopping parameter κ, required by the integration in the quark mass, on 6×48^3 lattices at one representative value of bare coupling and shift $L_0\boldsymbol{\xi} = (8a, 0, 0)$. We started from the ensemble at the lowest value of κ and we progressively increased it towards the critical value, exploring several algorithmic setups at each value of the hopping parameter. We defined a performance estimator given by the ratio of the computational time over acceptance rate; the best algorithm at given κ is the one that minimizes this estimator (with a lower bound of about 90% on the acceptance). We also monitored the spectrum of the Dirac operator so as to optimally tune the twisted masses for the Hasenbusch preconditioning and the RHMC parameters.

At the smallest values of hopping parameter we used a two-level multistep algorithm where the gauge force is at the finest level and the fermionic forces are at the coarsest one [74]. The latter include the contributions from the up-down doublet and from the RHMC for the strange quark. Both levels have been integrated with a fourth-order Omelyan-Mryglod-Folk (OMF) scheme [75], the finest with 1 step and the coarsest with a tunable number of steps ranging between 7 and 9 for increasing hopping parameter and decreasing temperature. By looking at the performance estimator introduced above and at the acceptance, we observed that the Hasenbusch preconditioning of the up-down doublet determinant is not required up to $\kappa \sim 0.10$. In the interval $0.10 \lesssim \kappa \lesssim 0.12$ this simple algorithm is refined with one Hasenbusch twisted mass equal to $\sqrt{\lambda_{\min}\lambda_{\max}}$ [76], where $\lambda_{\min}$ and $\lambda_{\max}$ are respectively the smallest and largest eigenvalues of the operator $\sqrt{D^\dagger D}$, whose determination is described later. In this interval the number of steps for the molecular dynamics at the coarsest level ranges between 9 and 15. For $\kappa \gtrsim 0.12$, we opted for a frequency splitting of the RHMC in two terms, and we added a third integration level to profit from the hierarchy in magnitude of these two contributions. The two finest levels have been integrated with 1 step of fourth-order OMF scheme, and the coarsest level with a second-order OMF scheme with a tunable number of steps from 12 to 17. More elaborated algorithms were not competitive up to $\kappa \gtrsim 0.126$, where we split the up-down doublet determinant with one further Hasenbusch twisted mass. We tried many setups, including a generalization of the rule proposed in Ref. [76] to the two twisted-mass case. At the end we found that the two values $\lambda_{\min} + \frac{1}{3}(\lambda_{\max} - \lambda_{\min})$ and $\lambda_{\max} - \frac{1}{3}(\lambda_{\max} - \lambda_{\min})$ are a good choice in terms of performance. Here the number of steps for the molecular dynamics at the coarsest level ranges between 13 and 20.

At a given L_0/a and g_0^2 we have measured $\lambda_{\min}$ and $\lambda_{\max}$ on the thermalization ensembles at several values of the hopping parameter and shift $\boldsymbol{\xi} = (1 + 2a/L_0, 0, 0)$. Figure 12 shows the lowest eigenvalue (left plot) and the largest one (right plot) as functions of κ for the temporal sizes $L_0/a = 6$, 10 and at the bare parameters of the temperatures T_1, T_8.

We have used these results also for the tuning of the rational approximation interval $[r_a, r_b]$ in the RHMC. At given bare parameters we have chosen the conservative values $r_a = 0.7\lambda_{\min}$ and $r_b = 1.2\lambda_{\max}$ to ensure that the spectrum of the Dirac operator is safely contained in the approximation interval. The number of poles ranges between 3 and 10 as $\lambda_{\min}$ decreases, and has been chosen so that the systematic error of the rational approximation is completely negligible within the final accuracy of the numerical results of the simulations [67,68].

2. Generation of ensembles

At each set of bare parameters $\{L_0/a, g_0^2, \kappa, \boldsymbol{\xi}\}$ the gauge configurations were first generated on lattices with spatial sizes $L/a = 48$, with a statistics of 500–1000 trajectories of 2 MDUs each. We have proceeded from high to low temperatures, using the last configuration of each ensemble as starting point for the ensemble at the same shift and closest hopping parameter at the next lower temperature. These small volume ensembles were used to test the performance of the algorithms, to measure the spectrum of the Dirac operator and to provide thermalization for the $L/a = 144$ ensembles. We have always monitored the components of the energy-momentum tensor and the $\mathbb{Z}_3$ phase of the generated configurations through the Polyakov loop. We have also monitored the Monte Carlo history of the average plaquette and of the topological charge at Wilson flow time $t_{\rm wf}$ fixed by the condition $T\sqrt{8t_{\rm wf}} = 1/\sqrt{10} \approx 0.3$ [77,78].

The lattices with target spatial size $L/a = 144$ were generated by tripling the $L/a = 48$ ones in the spatial directions, after verifying that the initial smaller-volume configuration was in the zero topological sector and had trivial $\mathbb{Z}_3$ phase. At the temperature T_8, resolution $L_0/a = 6$ and $\kappa \lesssim 0.10$, we further refined the thermalization

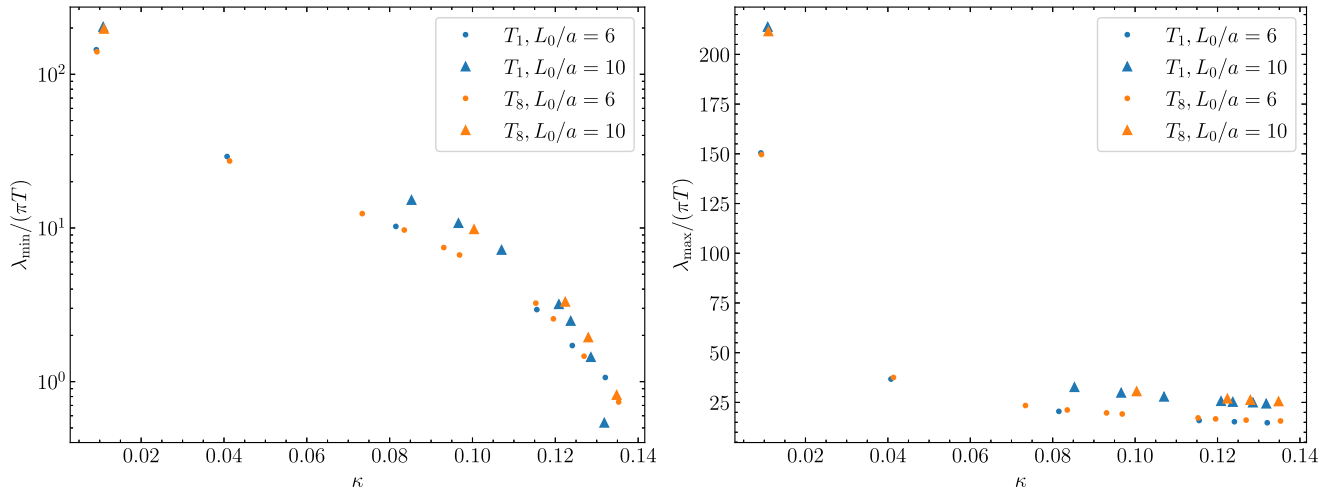

FIG. 12. Smallest (left plot) and largest (right plot) measured eigenvalues of the operator $\sqrt{D^\dagger D}$ as functions of the hopping parameter, at some representative values of temperature and lattice spacing.

procedure considering two steps: from $L/a = 24$ lattices to $L/a = 72$ ones and finally to the target volume by antiperiodically extending the $L/a = 72$ lattices to the $L/a = 144$ ones so as to start with exactly zero topology at the target volume. The Monte Carlo history of the average plaquette suggested to skip 50–100 trajectories as thermalization, after which we finally measured our observables. The same checks on energy-momentum tensor, topology and $\mathbb{Z}_3$ phase have been performed on the large volume ensembles as well.

APPENDIX F: SCALAR DENSITY VARIANCE REDUCTION

The scalar density is the primary observable for the computation of $\frac{\Delta(f_\xi - f_\xi^\infty)}{\Delta\xi_k}$. To optimize our numerical approach it is important to understand its behavior, and the one of its variance, in the limit of large values of the bare quark mass, i.e., their hopping parameter expansion.

1. Random sources

On a given gauge configuration, we estimate stochastically the trace of the quark propagator using U(1) random sources $\bar{\eta}, \eta$ [79–81], whose two-point function is

$$\langle \bar{\eta}^a_\alpha(x)\eta^b_\beta(y)\rangle = \delta_{xy}\delta^{ab}\delta_{\alpha\beta}, \tag{F1}$$

being x, y lattice sites, a, b color indices and α, β spin indices. Using this property it is immediate to show that

$$\mathcal{O}[U,\eta] = \frac{1}{N_s}\sum_{i=1}^{N_s}\frac{a^4}{V}\sum_x \bar{\eta}_i(x)\{S[U]\eta_i\}(x) \tag{F2}$$

is an estimator for the trace of the (single flavor) quark propagator $S = (D + m_0)^{-1}$. In this equation $V = L_0 L^3$ is the volume of the lattice and $\bar{\eta}_i, \eta_i$ are N_s independent random sources (spin and color indices have been omitted). Thus the expectation value of the scalar density can be written as follows:

$$a^3\langle\bar{\psi}\psi\rangle = -\frac{a^3}{V}N_f\langle \mathrm{Tr}\{S\}\rangle = -a^{-1}N_f\langle\mathcal{O}\rangle, \tag{F3}$$

where the trace $\mathrm{Tr}\{\cdot\}$ is over spacetime, spin and color indices and $N_f = 3$ in our case. The variance of $\mathcal{O}$ reads

$$\frac{V^2}{a^8}(\langle\mathcal{O}^2\rangle - \langle\mathcal{O}\rangle^2) = [\langle \mathrm{Tr}^2\{S\}\rangle - \langle\mathrm{Tr}\{S\}\rangle^2] + \frac{1}{N_s}\left[\langle\mathrm{Tr}\{S^2\}\rangle - \left\langle\sum_{x,c,\sigma}[S^{cc}_{\sigma\sigma}(x,x)]^2\right\rangle\right], \tag{F4}$$

where the term in the first square brackets is the gauge noise, while the term in the second square brackets is the additional noise due to the use of random sources. The computation of Eq. (F4) involves a four-point function of the random sources, whose expression for U(1) fields is

$$\langle\bar{\eta}^a_\alpha(x)\eta^b_\beta(y)\bar{\eta}^c_\gamma(z)\eta^d_\delta(w)\rangle = \delta_{xy}\delta_{zw}\delta^{ab}\delta^{cd}\delta_{\alpha\beta}\delta_{\gamma\delta} + \delta_{xw}\delta_{yz}\delta^{ad}\delta^{bc}\delta_{\alpha\delta}\delta_{\beta\gamma} - \delta_{xyzw}\delta^{abcd}\delta_{\alpha\beta\gamma\delta}. \tag{F5}$$

2. Hopping parameter expansion

To study the large mass behavior it is convenient to rewrite the operator $D + m_0$ as follows:

$$D + m_0 = H + \frac{1}{2a\kappa}, \qquad H \equiv D - \frac{4}{a}, \tag{F6}$$

where H includes the hopping terms of the Wilson-Dirac operator D_w and the improvement operator aD_sw, and

$\kappa = 1/(8 + 2am_0)$ is the hopping parameter. In the $\kappa \to 0$ expansion, the quark propagator reads

$$a^{-1}S = \frac{2\kappa}{1 + 2\kappa aH} = 2\kappa \sum_{n=0}^{\infty} (-2\kappa aH)^n. \tag{F7}$$

We are interested in the computation of the shift derivative of the expectation value of the scalar density, see Eq. (11). Its hopping expansion at leading order is

$$a^3 \frac{\Delta\langle\bar{\psi}\psi\rangle_\xi}{\Delta\xi_k} = -8\kappa^3 \frac{a^4}{V} N_f \frac{\Delta\langle T_2\rangle_\xi}{\Delta\xi_k} + O(\kappa^4), \tag{F8}$$

where we introduced the convenient notation

$$T_n \equiv \mathrm{Tr}\{(aH)^n\} = a^n \sum_{x,c,\sigma} (H^n)^{cc}_{\sigma\sigma}(x,x). \tag{F9}$$

On the other hand, the hopping expansion of the variance of the estimator $\mathcal{O}$ is

$$\begin{aligned}
&\frac{V^2}{a^{10}}(\langle\mathcal{O}^2\rangle - \langle\mathcal{O}\rangle^2) \\
&= (2\kappa)^6[\langle T_2^2\rangle - \langle T_2\rangle^2 + O(\kappa)] \\
&\quad + \frac{1}{N_s}(2\kappa)^4\left[\langle T_2\rangle - \left\langle \sum_{x,c,\sigma}[aH^{cc}_{\sigma\sigma}(x,x)]^2\right\rangle + O(\kappa)\right],
\end{aligned} \tag{F10}$$

where the $O(\kappa^6)$ contribution comes from the fluctuations of the gauge configurations only, while the $O(\kappa^4)$ contribution originates from the presence of random sources. Therefore, the leading scaling of the overall variance in the hopping expansion is of $O(\kappa^4)$. As a consequence, the signal-to-noise ratio of the quantity in Eq. (F8) is of $O(\kappa)$ and decreases for increasing quark mass values. The slower decreasing of the $O(\kappa^4)$ contribution in Eq. (F10) may be compensated by increasing the number of sources as $N_s \propto \kappa^{-2}$, although this would make the computation more and more demanding as $\kappa \to 0$.

3. Hopping subtraction

Following Ref. [25] we have introduced an improved version of the estimator, called $\tilde{\mathcal{O}}$, obtained by replacing

$$S \to S + 4\kappa^2 a^2 H \tag{F11}$$

in the definition Eq. (F2), i.e., the quark propagator is subtracted by its leading nontrivial order in the hopping parameter expansion. Since H is traceless, the expectation values of the original estimator and of the improved one coincide: $\langle\mathcal{O}\rangle = \langle\tilde{\mathcal{O}}\rangle$. The subtraction removes the leading $O(\kappa^4)$ terms in the hopping expansion of the variance so that the total variance is now of $O(\kappa^6)$,

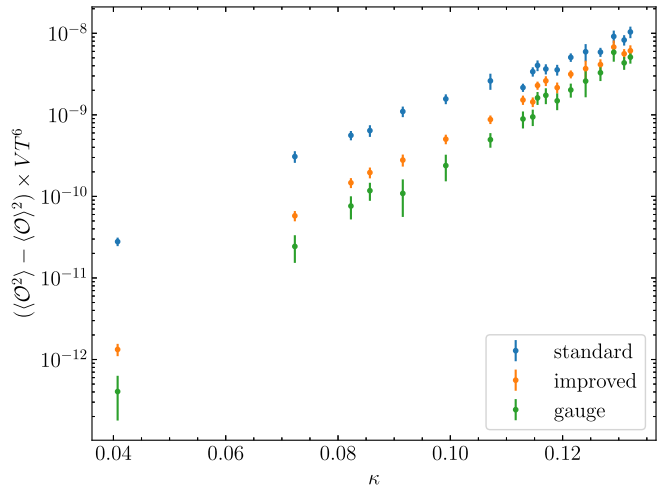

FIG. 13. Variance computed with the estimators $\mathcal{O}$ (blue points) and $\tilde{\mathcal{O}}$ (orange points), respectively defined in Eqs. (F2) and (F11). For comparison, the gauge contribution is also shown (green points). These data are a representative case obtained from 6×144^3 lattices at inverse bare coupling $6/g_0^2 = 8.5403$.

$$\begin{aligned}
\frac{V^2}{a^{10}}(\langle\tilde{\mathcal{O}}^2\rangle - \langle\tilde{\mathcal{O}}\rangle^2) = (2\kappa)^6 \Bigg[\langle T_2^2\rangle - \langle T_2\rangle^2 + \frac{1}{N_s}\Bigg(\langle T_4\rangle \\
- \left\langle \sum_{x,c,\sigma}[(a^2H^2)^{cc}_{\sigma\sigma}(x,x)]^2\right\rangle\Bigg)\Bigg] \\
+ O(\kappa^7),
\end{aligned} \tag{F12}$$

and the signal-to-noise ratio of the derivative in Eq. (F8) is consequently of $O(1)$ in the hopping parameter. The effect of the improvement can be seen in Fig. 13, where the comparison of the variance computed with the standard estimator in Eq. (F2) and with the improved one through Eq. (F11) is shown, at several values of the hopping parameter. The variance of the improved estimator is smaller than the one of the standard definition at all values of κ considered, and for $\kappa \to 0$ the former decreases faster than the latter with a trend very similar to the one of the gauge noise component, which is shown in the plot as well.

This simple subtraction leads to a factor up to 2.5 gain in the statistical error of $\frac{\Delta(f_\xi - f_\xi^\infty)}{\Delta\xi_k}$ with negligible additional computational cost, as the effort of evaluating numerically the estimators $\tilde{\mathcal{O}}$ and $\mathcal{O}$ on a given gauge configuration is by far dominated by the computation of the quark propagator.

APPENDIX G: OPTIMIZATION OF THE STATISTICS

We discuss here the strategy that we have implemented for the optimization of the statistics needed for the numerical determination of $\frac{\Delta(f_\xi - f_\xi^\infty)}{\Delta\xi_k}$, computed as described in Sec. IV. At a given set of bare parameters L_0/a and g_0^2 the error squared of this contribution is propagated from the

fluctuations of the scalar density as follows:

$$\sigma^2\left[\frac{1}{T^4}\frac{\Delta(f_\xi - f_\xi^\infty)}{\Delta\xi_k}\right] = \sum_{k=1}^{n_G}\omega_k^2\sigma^2\left[\frac{1}{T^3}\frac{\Delta\langle\bar\psi\psi\rangle_\xi^{m_{q,k}}}{\Delta\xi_k}\right], \qquad \text{(G1)}$$

where the index k runs over the $n_G = 20$ Gauss points prescribed by the integration scheme of Eq. (14), ω_k are the related Gauss weights and on the right it appears the error squared of the discrete derivative of $\langle\bar\psi\psi\rangle_\xi^{m_q}$ with respect to the shift. The latter is obtained as the sum in quadrature of the errors at the same bare quark mass and two shifts. The contribution to the final error of the different Gauss points is thus modulated by the square of the Gauss weights ω_k^2, whose magnitude is maximum in the middle of the integration intervals and decreases symmetrically towards the boundaries. This suggests that the number of measurements of the scalar density at different bare quark masses can be tuned so as to minimize the computational cost for attaining a given target accuracy. In this optimization we also considered that the computational cost of simulations and the variance of the observable depend on the bare quark mass.

TABLE X. Number of measurements for each L_0/a optimized to obtain $\frac{\Delta(f_\xi - f_\xi^\infty)}{\Delta\xi_k}$ with a 0.5% relative error for $L_0/a = 4, 6, 8$ and a 1.0% relative error for $L_0/a = 10$, at the temperature T_1 and $L/a = 144$. Each row corresponds to one of the Gauss quadrature points for the numerical determination of the integral in the bare quark mass, and they are labeled by the index k as in Eq. (G1). The bare subtracted quark mass increases from top to bottom. Horizontal lines separate the three integration domains as described in Eq. (14).

k	$L_0/a = 4$	$L_0/a = 6$	$L_0/a = 8$	$L_0/a = 10$
1	50	100	50	50
2	50	100	150	100
3	50	100	150	100
4	50	100	200	200
5	50	100	150	250
6	50	100	150	250
7	50	100	150	200
8	50	100	150	150
9	50	100	100	100
10	50	100	50	50
11	50	100	250	300
12	50	100	400	600
13	50	100	450	700
14	50	100	400	700
15	50	100	300	500
16	50	100	150	350
17	50	100	150	150
18	50	100	1400	2400
19	50	100	1200	2100
20	50	100	150	300

Therefore, at fixed L_0/a and g_0^2 the quantity to be minimized is the total computational cost, under the constraint that the final relative error on $\frac{\Delta(f_\xi - f_\xi^\infty)}{\Delta\xi_k}$ is equal to a target value. This problem can be solved through the method of Lagrange multipliers, the variables to be optimized being the number of measurements for the determination of $\langle\bar\psi\psi\rangle_\xi^{m_q}$ at the different Gauss points. We have chosen a target relative accuracy of 0.5% at $L_0/a = 4, 6, 8$ and 1.0% at $L_0/a = 10$. As an example, the optimized results for the temperature T_1 are reported in Table X. At the other temperatures, we increased these optimized numbers by a monotonically growing factor up to 2 at the lowest temperature. The quoted numbers of measurements refer to both shifts. For the coarsest resolutions $L_0/a = 4, 6$ there was little gain from this procedure, thus we have chosen a fixed number of measurements for all the Gauss quadrature points. We have used the optimization for the finest lattices $L_0/a = 8, 10$ which are the most expensive to be generated. The gain in computational cost is up to a factor 2 in comparison with the case where the same number of measurements is chosen for all the Gauss quadrature points, at the same fixed target accuracy. We have also generalized this procedure so as to optimize the number of sampled noise sources (see Appendix F) as well, but the latter turned out to be mostly constant and for convenience we have fixed it to 100 for all the simulations.

APPENDIX H: FURTHER NUMERICAL RESULTS

In this appendix we collect some auxiliary numerical results which complement the ones given in the main text.

1. Results for $\frac{\Delta\langle\overline{S_G}\rangle_\xi^\infty}{\Delta\xi_k}$

As a representative case, we give in Table XI the numerical results for the derivative in the shift of the expectation value of the density of the Wilson plaquette action, defined in Eq. (A1), computed in pure gauge simulations at the lattice resolution $L_0/a = 6$ and at the values of bare coupling prescribed by the integration scheme presented in Sec. IV.

2. Results for $\frac{\Delta\langle\bar\psi\psi\rangle_\xi^{m_q}}{\Delta\xi_k}$

As a representative case we collect in Table XII the results for the derivative in the shift of the expectation value of the scalar density defined in Eq. (F3) computed in lattice QCD simulations with $L_0/a = 6$ and $6/g_0^2 = 8.5403$ (corresponding to the temperature T_1), at the hopping parameter values prescribed by the integration scheme presented in Sec. IV.

3. Covariance of continuum limit results

We report in Table XIII the entries of the covariance matrix of the continuum limits c_i, $i = 0, \ldots, 8$ of the best-fit `id3` in Table V, each normalized to the product of the errors. We also give the normalized covariance values of the

TABLE XI. Numerical results for $\frac{\Delta\langle\overline{S_G}\rangle_{\xi}^{\infty}}{\Delta\xi_k}$ computed on 6×144^3 lattices at the given values of inverse bare coupling $6/g_0^2$. Horizontal lines indicate the grouping of bare couplings according to the integration scheme in Table II.

$6/g_0^2$	$\frac{\Delta\langle\overline{S_G}\rangle_{\xi}^{\infty}}{\Delta\xi_k}\times 10^4$	$6/g_0^2$	$\frac{\Delta\langle\overline{S_G}\rangle_{\xi}^{\infty}}{\Delta\xi_k}\times 10^4$
15.0000	0.22(3)	7.5523	2.71(9)
13.9517	0.21(5)	7.4227	3.15(7)
11.2500	0.32(5)	7.2975	3.76(9)
9.4249	0.56(7)	7.2245	4.13(8)
8.9975	0.83(6)	7.0990	4.95(6)
8.9457	0.84(6)	6.9778	5.80(9)
8.7641	0.97(5)	6.9267	6.41(9)
8.5897	1.12(5)	6.8622	7.16(6)
8.5026	1.12(4)	6.7699	8.46(8)
8.3755	1.24(4)	6.6801	10.24(17)
8.2522	1.44(6)	6.6201	11.61(14)
8.1811	1.49(5)	6.5887	12.49(25)
8.0601	1.69(5)	6.5254	14.55(29)
7.9426	1.78(5)	6.4350	18.9(4)
7.8719	1.96(7)	6.3470	25.9(5)
7.7467	2.23(6)	6.2883	34.5(7)
7.6255	2.56(9)		

continuum limits c_i with the coefficient d_{23} which parametrizes the discretization effects,

$$\frac{\mathrm{cov}(c_i, d_{23})}{\sigma(c_i)\sigma(d_{23})} = (-0.613, -0.683, -0.701, -0.702, -0.716, -0.721, -0.754, -0.731, -0.737). \tag{H1}$$

TABLE XII. Numerical results for $\frac{\Delta\langle\bar{\psi}\psi\rangle_{\xi}}{\Delta\xi_k}$ computed on 6×144^3 lattices at inverse bare coupling $6/g_0^2 = 8.5403$ and at the given values of hopping parameter κ. Horizontal lines indicate the three sets of 10, 6, and 3 Gauss points according to the integration scheme described in Sec. IV B.

κ	$\frac{\Delta\langle\bar{\psi}\psi\rangle_{\xi}}{\Delta\xi_k}\times 10^3$	κ	$\frac{\Delta\langle\bar{\psi}\psi\rangle_{\xi}}{\Delta\xi_k}\times 10^3$
0.132067	−0.491(14)	0.112938	−0.770(7)
0.130958	−1.457(13)	0.107136	−0.3191(29)
0.129108	−2.608(13)	0.099197	−0.0962(28)
0.126736	−3.132(10)	0.091536	−0.0279(21)
0.124100	−2.888(8)	0.085678	−0.0133(15)
0.121455	−2.299(8)	0.082296	−0.0073(16)
0.119031	−1.757(8)	0.072311	−0.0006(8)
0.117012	−1.346(6)	0.040748	−0.00015(11)
0.115533	−1.115(6)	0.009185	−0.0000001(14)
0.114683	−0.990(5)		

TABLE XIII. Entries of the covariance matrix $\mathrm{cov}(c_i, c_j)$ of the continuum results of the best-fit id3 in Table V, normalized to the product of the errors $\sigma(c_i)$ and $\sigma(c_j)$.

(i,j)	$\frac{\mathrm{cov}(c_i,c_j)}{\sigma(c_i)\sigma(c_j)}$	(i,j)	$\frac{\mathrm{cov}(c_i,c_j)}{\sigma(c_i)\sigma(c_j)}$	(i,j)	$\frac{\mathrm{cov}(c_i,c_j)}{\sigma(c_i)\sigma(c_j)}$
(0, 1)	0.687	(1, 6)	0.775	(3, 7)	0.765
(0, 2)	0.690	(1, 7)	0.755	(3, 8)	0.763
(0, 3)	0.688	(1, 8)	0.753	(4, 5)	0.774
(0, 4)	0.696	(2, 3)	0.757	(4, 6)	0.796
(0, 5)	0.696	(2, 4)	0.766	(4, 7)	0.775
(0, 6)	0.707	(2, 5)	0.766	(4, 8)	0.774
(0, 7)	0.700	(2, 6)	0.787	(5, 6)	0.797
(0, 8)	0.696	(2, 7)	0.766	(5, 7)	0.776
(1, 2)	0.750	(2, 8)	0.763	(5, 8)	0.775
(1, 3)	0.747	(3, 4)	0.764	(6, 7)	0.799
(1, 4)	0.756	(3, 5)	0.764	(6, 8)	0.798
(1, 5)	0.755	(3, 6)	0.785	(7, 8)	0.781

APPENDIX I: EVALUATION OF THE $\overline{\mathrm{MS}}$ STRONG COUPLING AT FIVE-LOOP ORDER

In this appendix we collect the details for the computation of the renormalized coupling $\hat{g}$, appearing in Secs. V and VI. It is defined as the five-loop $\overline{\mathrm{MS}}$ coupling for QCD with $N_f = 3$ flavors, evaluated at the renormalization scale $\mu = 2\pi T$. The Λ-parameter in this scheme is defined by [16]

$$\Lambda_{\overline{\mathrm{MS}}} = \mu\varphi(\hat{g}(\mu/\Lambda_{\overline{\mathrm{MS}}})), \tag{I1}$$

where the function $\varphi(\hat{g})$ is

$$\varphi(\hat{g}) = (b_0\hat{g}^2)^{-b_1/(2b_0^2)} e^{-1/(2b_0\hat{g}^2)} e^{-\mathcal{I}_\beta(\hat{g})} \tag{I2}$$

with

$$\mathcal{I}_\beta(\hat{g}) = \int_0^{\hat{g}} dg \left[\frac{1}{\beta(g)} + \frac{1}{b_0 g^3} - \frac{b_1}{b_0^2 g}\right], \tag{I3}$$

and the β-function is expanded in perturbation theory as follows:

$$\beta(\hat{g}) = \mu\frac{\partial\hat{g}}{\partial\mu} \overset{\hat{g}\to 0}{\to} -\hat{g}^3\sum_{k\geq 0} b_k\hat{g}^{2k}. \tag{I4}$$

The perturbative coefficients b_k are related to the coefficients β_k, $k = 0, 1, 2, 3, 4$, determined in Ref. [34], by the relation

$$b_k = \frac{\beta_k}{(2\pi)^{2k+2}}. \tag{I5}$$

We report here the values for the two lowest orders, which do not depend on the renormalization scheme,

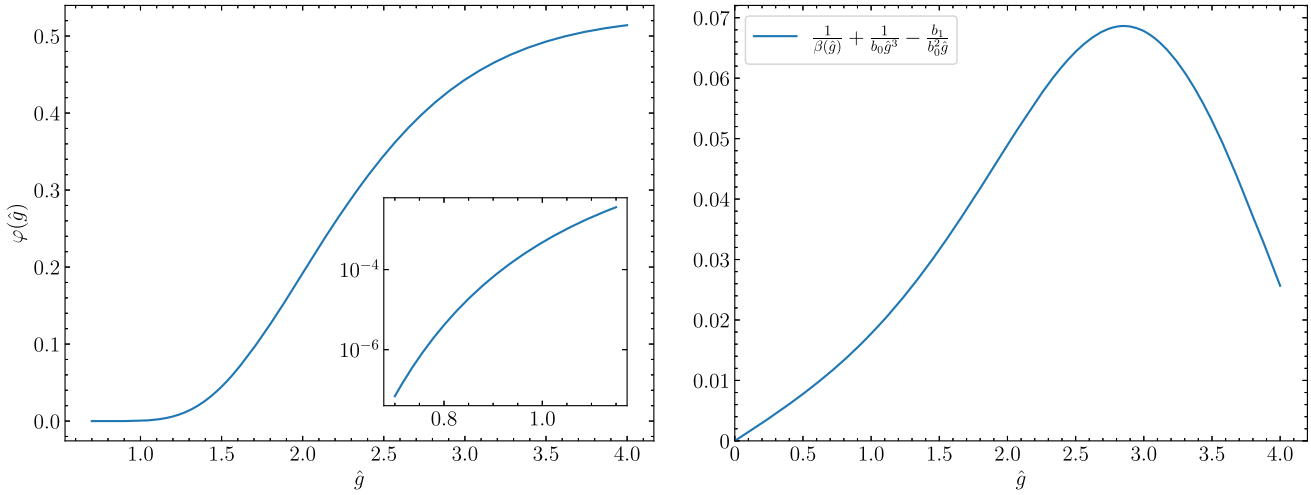

FIG. 14. Left: Plot of the function φ in Eq. (I2). The smaller plot is a detail for the interval $0.8 \lesssim \hat{g} \lesssim 1.1$, with log scale on the y-axis. Right: Plot of the integrand function of $\mathcal{I}_\beta(\hat{g})$ in Eq. (I3).

$$\beta_0 = \frac{1}{4}\left(11 - \frac{2}{3}N_f\right), \qquad \beta_1 = \frac{1}{16}\left(102 - \frac{38}{3}N_f\right). \quad \text{(I6)}$$

At a given value of $\mu/\Lambda_{\overline{\mathrm{MS}}}$, we have computed the corresponding coupling $\hat{g}(\mu/\Lambda_{\overline{\mathrm{MS}}})$ by solving numerically Eq. (I1). The evaluation of the function $\varphi(\hat{g})$, represented in the left panel of Fig. 14, requires the computation of the integral $\mathcal{I}_\beta(\hat{g})$. To this purpose, we have used the optimized QUADPACK quadrature routines [82] on the integrand function, plotted in the right panel of Fig. 14. We have restricted the numerical approach to the conservative domain $2 \le \mu/\Lambda_{\overline{\mathrm{MS}}} \le 10^5$, corresponding to $0.8 \lesssim \hat{g} \lesssim 3.6$. This interval largely includes all the values of energy scale and renormalized coupling we are interested in. Some representative results at several renormalization scales are reported in Table XIV.

TABLE XIV. Results for the running coupling $\hat{g}$ at some values of the renormalization scale.

$\mu/\Lambda_{\overline{\mathrm{MS}}}$	$\hat{g}(\mu/\Lambda_{\overline{\mathrm{MS}}})$
2	3.62600
10^1	1.71582
10^2	1.25818
10^3	1.04760
10^4	0.91833
10^5	0.82827

For $\mu/\Lambda_{\overline{\mathrm{MS}}} > 10^5$, we have switched to the three-loop analytic formula obtained from Ref. [83]. The two couplings at the scale $\mu/\Lambda_{\overline{\mathrm{MS}}} = 10^5$ differ by less than 0.03%, and the discrepancy is expected to decrease as the renormalization scale increases.

[1] K. Saikawa and S. Shirai, Primordial gravitational waves, precisely: The role of thermodynamics in the standard model, J. Cosmol. Astropart. Phys. 05 (2018) 035.
[2] K. Saikawa and S. Shirai, Precise WIMP dark matter abundance and standard model thermodynamics, J. Cosmol. Astropart. Phys. 08 (2020) 011.
[3] S. Acharya *et al.* (ALICE Collaboration), Two-particle transverse momentum correlations in pp and p-Pb collisions at LHC energies, Phys. Rev. C **107**, 054617 (2023).
[4] M. Gyulassy and L. McLerran, New forms of QCD matter discovered at RHIC, Nucl. Phys. **A750**, 30 (2005).
[5] M. Bresciani, M. Dalla Brida, L. Giusti, and M. Pepe, QCD equation of state with $N_f = 3$ flavors up to the electroweak scale, Phys. Rev. Lett. **134**, 201904 (2025).
[6] L. Giusti and M. Pepe, Equation of state of the SU(3) Yang–Mills theory: A precise determination from a moving frame, Phys. Lett. B **769**, 385 (2017).
[7] L. Giusti and H. B. Meyer, Thermal momentum distribution from path integrals with shifted boundary conditions, Phys. Rev. Lett. **106**, 131601 (2011).
[8] L. Giusti and H. B. Meyer, Thermodynamic potentials from shifted boundary conditions: The scalar-field theory case, J. High Energy Phys. 11 (2011) 087.

[9] L. Giusti and H. B. Meyer, Implications of Poincaré symmetry for thermal field theories in finite-volume, J. High Energy Phys. 01 (2013) 140.

[10] M. Dalla Brida, L. Giusti, and M. Pepe, Non-perturbative definition of the QCD energy-momentum tensor on the lattice, J. High Energy Phys. 04 (2020) 043.

[11] K. G. Wilson, Confinement of quarks, Phys. Rev. D **10**, 2445 (1974).

[12] K. G. Wilson, Quarks: From paradox to myth, Subnucl. Ser. **13**, 13 (1977).

[13] B. Sheikholeslami and R. Wohlert, Improved continuum limit lattice action for QCD with Wilson fermions, Nucl. Phys. **B259**, 572 (1985).

[14] M. Dalla Brida, L. Giusti, T. Harris, D. Laudicina, and M. Pepe, Non-perturbative thermal QCD at all temperatures: The case of mesonic screening masses, J. High Energy Phys. 04 (2022) 034.

[15] I. Campos, P. Fritzsch, C. Pena, D. Preti, A. Ramos, and A. Vladikas (ALPHA Collaboration), Non-perturbative quark mass renormalisation and running in $N_f = 3$ QCD, Eur. Phys. J. C **78**, 387 (2018).

[16] M. Dalla Brida, P. Fritzsch, T. Korzec, A. Ramos, S. Sint, and R. Sommer (ALPHA Collaboration), A non-perturbative exploration of the high energy regime in $N_\mathrm{f} = 3$ QCD, Eur. Phys. J. C **78**, 372 (2018).

[17] M. Bruno, M. Dalla Brida, P. Fritzsch, T. Korzec, A. Ramos, S. Schaefer, H. Simma, S. Sint, and R. Sommer (ALPHA Collaboration), QCD coupling from a nonperturbative determination of the three-flavor Λ parameter, Phys. Rev. Lett. **119**, 102001 (2017).

[18] M. Dalla Brida, P. Fritzsch, T. Korzec, A. Ramos, S. Sint, and R. Sommer (ALPHA Collaboration), Determination of the QCD Λ-parameter and the accuracy of perturbation theory at high energies, Phys. Rev. Lett. **117**, 182001 (2016).

[19] L. Giusti and M. Pepe, Energy-momentum tensor on the lattice: Nonperturbative renormalization in Yang-Mills theory, Phys. Rev. D **91**, 114504 (2015).

[20] L. Giusti, M. Hirasawa, M. Pepe, and L. Virzì, A precise study of the thermodynamic properties of the SU(3) Yang-Mills theory across the deconfinement transition, Phys. Lett. B **868**, 139775 (2025).

[21] S. L. Adler, Overrelaxation algorithms for lattice field theories, Phys. Rev. D **37**, 458 (1988).

[22] N. Cabibbo and E. Marinari, A new method for updating $\mathrm{SU}(N)$ matrices in computer simulations of gauge theories, Phys. Lett. B **119**, 387 (1982).

[23] M. Creutz, Confinement and the critical dimensionality of space-time, Phys. Rev. Lett. **43**, 553 (1979); **43**, 890(E) (1979).

[24] M. Creutz, Monte Carlo study of quantized SU(2) gauge theory, Phys. Rev. D **21**, 2308 (1980).

[25] L. Giusti, T. Harris, A. Nada, and S. Schaefer, Frequency-splitting estimators of single-propagator traces, Eur. Phys. J. C **79**, 586 (2019).

[26] U. Wolff (ALPHA Collaboration), Monte Carlo errors with less errors, Comput. Phys. Commun. **156**, 143 (2004); **176**, 383(E) (2007).

[27] F. Joswig, S. Kuberski, J. T. Kuhlmann, and J. Neuendorf, PYERRORS: A Python framework for error analysis of Monte Carlo data, Comput. Phys. Commun. **288**, 108750 (2023).

[28] A. Ramos, Automatic differentiation for error analysis of Monte Carlo data, Comput. Phys. Commun. **238**, 19 (2019).

[29] M. Laine and M. Vepsalainen, On the smallest screening masses in hot QCD, J. High Energy Phys. 09 (2009) 023.

[30] L. Giusti and M. Lüscher, Topological susceptibility at $T > T_\mathrm{c}$ from master-field simulations of the SU(3) gauge theory, Eur. Phys. J. C **79**, 207 (2019).

[31] S. Borsanyi *et al.*, Calculation of the axion mass based on high-temperature lattice quantum chromodynamics, Nature (London) **539**, 69 (2016).

[32] A. Bazavov, P. Petreczky, and J. H. Weber, Equation of state in $2+1$ flavor QCD at high temperatures, Phys. Rev. D **97**, 014510 (2018).

[33] M. Bruno and R. Sommer, On fits to correlated and auto-correlated data, Comput. Phys. Commun. **285**, 108643 (2023).

[34] P. A. Baikov, K. G. Chetyrkin, and J. H. Kühn, Five-loop running of the QCD coupling constant, Phys. Rev. Lett. **118**, 082002 (2017).

[35] N. Husung, P. Marquard, and R. Sommer, Asymptotic behavior of cutoff effects in Yang–Mills theory and in Wilson's lattice QCD, Eur. Phys. J. C **80**, 200 (2020).

[36] N. Husung, P. Marquard, and R. Sommer, The asymptotic approach to the continuum of lattice QCD spectral observables, Phys. Lett. B **829**, 137069 (2022).

[37] N. Husung, Logarithmic corrections to O(a) and $O(a^2)$ effects in lattice QCD with Wilson or Ginsparg–Wilson quarks, Eur. Phys. J. C **83**, 142 (2023).

[38] K. Kajantie, M. Laine, K. Rummukainen, and Y. Schroder, The pressure of hot QCD up to $g^6 \ln(1/g)$, Phys. Rev. D **67**, 105008 (2003).

[39] E. V. Shuryak, Theory of hadronic plasma, Sov. Phys. JETP **47**, 212 (1978), https://jetp.ras.ru/cgi-bin/e/index/e/47/2/p212?a=list.

[40] S. A. Chin, Transition to hot quark matter in relativistic heavy ion collision, Phys. Lett. **78B**, 552 (1978).

[41] J. I. Kapusta, Quantum chromodynamics at high temperature, Nucl. Phys. **B148**, 461 (1979).

[42] T. Toimela, The next term in the thermodynamic potential of QCD, Phys. Lett. **124B**, 407 (1983).

[43] P. B. Arnold and C.-X. Zhai, The three loop free energy for pure gauge QCD, Phys. Rev. D **50**, 7603 (1994).

[44] P. B. Arnold and C.-x. Zhai, The three loop free energy for high temperature QED and QCD with fermions, Phys. Rev. D **51**, 1906 (1995).

[45] C.-x. Zhai and B. M. Kastening, The free energy of hot gauge theories with fermions through g^5, Phys. Rev. D **52**, 7232 (1995).

[46] A. D. Linde, Infrared problem in thermodynamics of the Yang-Mills gas, Phys. Lett. **96B**, 289 (1980).

[47] D. J. Gross, R. D. Pisarski, and L. G. Yaffe, QCD and instantons at finite temperature, Rev. Mod. Phys. **53**, 43 (1981).

[48] P. Navarrete and Y. Schröder, The g^6 pressure of hot Yang-Mills theory: Canonical form of the integrand, J. High Energy Phys. 11 (2024) 037.

[49] S. Borsanyi, Z. Fodor, C. Hoelbling, S. D. Katz, S. Krieg, and K. K. Szabo, Full result for the QCD equation of state with $2+1$ flavors, Phys. Lett. B **730**, 99 (2014).

[50] A. Bazavov *et al.* (HotQCD Collaboration), Equation of state in $(2+1)$-flavor QCD, Phys. Rev. D **90**, 094503 (2014).

[51] M. Laine and Y. Schroder, Quark mass thresholds in QCD thermodynamics, Phys. Rev. D **73**, 085009 (2006).

[52] J. O. Andersen, E. Petitgirard, and M. Strickland, Two loop HTL thermodynamics with quarks, Phys. Rev. D **70**, 045001 (2004).

[53] J. O. Andersen, M. Strickland, and N. Su, Three-loop HTL gluon thermodynamics at intermediate coupling, J. High Energy Phys. 08 (2010) 113.

[54] J. O. Andersen, L. E. Leganger, M. Strickland, and N. Su, Three-loop HTL QCD thermodynamics, J. High Energy Phys. 08 (2011) 053.

[55] L. Fernandez and J.-L. Kneur, Renormalization group optimized $\lambda\phi^4$ pressure at next-to-next-to-leading order, Phys. Rev. D **104**, 096012 (2021).

[56] S. Caracciolo, G. Curci, P. Menotti, and A. Pelissetto, The energy momentum tensor for lattice gauge theories, Ann. Phys. (N.Y.) **197**, 119 (1990).

[57] S. Caracciolo, G. Curci, P. Menotti, and A. Pelissetto, Renormalization of the energy momentum tensor and the trace anomaly in lattice QED, Phys. Lett. B **228**, 375 (1989).

[58] S. Caracciolo, P. Menotti, and A. Pelissetto, Analytic determination at one loop of the energy momentum tensor for lattice QCD, Phys. Lett. B **260**, 401 (1991).

[59] S. Caracciolo, P. Menotti, and A. Pelissetto, One loop analytic computation of the energy momentum tensor for lattice gauge theories, Nucl. Phys. **B375**, 195 (1992).

[60] N. Yamada *et al.* (JLQCD, CP-PACS Collaborations), Non-perturbative O(a)-improvement of Wilson quark action in three-flavor QCD with plaquette gauge action, Phys. Rev. D **71**, 054505 (2005).

[61] M. Lüscher, S. Sint, R. Sommer, and P. Weisz, Chiral symmetry and O(a) improvement in lattice QCD, Nucl. Phys. **B478**, 365 (1996).

[62] S. Kurth, The renormalized quark mass in the Schrödinger functional of lattice QCD: A one loop calculation with a nonvanishing background field, Ph.D. thesis, Humboldt University, Berlin, 2002, arXiv:hep-lat/0211011.

[63] H. Panagopoulos and Y. Proestos, The critical hopping parameter in O(a) improved lattice QCD, Phys. Rev. D **65**, 014511 (2002).

[64] M. Lüscher and P. Weisz, Coordinate space methods for the evaluation of Feynman diagrams in lattice field theories, Nucl. Phys. **B445**, 429 (1995).

[65] M. Abramowitz and I. A. Stegun, *Handbook of Mathematical Functions: With Formulas, Graphs, and Mathematical Tables* (Courier Corporation, New York, 1965), Vol. 55.

[66] P. Rabinowitz, The exact degree of precision of generalized Gauss-Kronrod integration rules, Math. Comput. **35**, 1275 (1980).

[67] M. Lüscher, openQCD: Simulation programs for lattice QCD, https://luscher.web.cern.ch/luscher/openQCD/.

[68] M. Lüscher and S. Schaefer, Lattice QCD with open boundary conditions and twisted-mass reweighting, Comput. Phys. Commun. **184**, 519 (2013).

[69] M. Dalla Brida, L. Giusti, and M. Pepe, QCD in a moving frame: An exploratory study, EPJ Web Conf. **175**, 14012 (2018).

[70] M. Hasenbusch, Speeding up the hybrid Monte Carlo algorithm for dynamical fermions, Phys. Lett. B **519**, 177 (2001).

[71] A. D. Kennedy, I. Horvath, and S. Sint, A new exact method for dynamical fermion computations with nonlocal actions, Nucl. Phys. B, Proc. Suppl. **73**, 834 (1999).

[72] M. A. Clark and A. D. Kennedy, The RHMC algorithm for two flavors of dynamical staggered fermions, Nucl. Phys. B, Proc. Suppl. **129**, 850 (2004).

[73] M. Lüscher, Computational Strategies in Lattice QCD, in *Les Houches Summer School: Session 93: Modern Perspectives in Lattice QCD: Quantum Field Theory and High Performance Computing* (2010), pp. 331–399; arXiv:1002.4232.

[74] J. C. Sexton and D. H. Weingarten, Hamiltonian evolution for the hybrid Monte Carlo algorithm, Nucl. Phys. **B380**, 665 (1992).

[75] I. P. Omelyan, I. M. Mryglod, and R. Folk, Symplectic analytically integrable decomposition algorithms: Classification, derivation, and application to molecular dynamics, quantum and celestial mechanics simulations, Comput. Phys. Commun. **151**, 272 (2003).

[76] M. Hasenbusch and K. Jansen, Speeding up lattice QCD simulations with clover improved Wilson fermions, Nucl. Phys. **B659**, 299 (2003).

[77] P. Fritzsch, A. Ramos, and F. Stollenwerk, Critical slowing down and the gradient flow coupling in the Schrödinger functional, Proc. Sci. Lattice2013 (**2014**) 461 [arXiv:1311.7304].

[78] M. Dalla Brida, P. Fritzsch, T. Korzec, A. Ramos, S. Sint, and R. Sommer (ALPHA Collaboration), Slow running of the gradient flow coupling from 200 MeV to 4 GeV in $N_f = 3$ QCD, Phys. Rev. D **95**, 014507 (2017).

[79] K. Bitar, A. D. Kennedy, R. Horsley, S. Meyer, and P. Rossi, The QCD finite temperature transition and hybrid Monte Carlo, Nucl. Phys. **B313**, 348 (1989).

[80] S.-J. Dong and K.-F. Liu, Stochastic estimation with Z(2) noise, Phys. Lett. B **328**, 130 (1994).

[81] C. Michael and J. Peisa (UKQCD Collaboration), Maximal variance reduction for stochastic propagators with applications to the static quark spectrum, Phys. Rev. D **58**, 034506 (1998).

[82] R. Piessens, E. de Doncker-Kapenga, C. W. Überhuber, and D. Kahaner, *QUADPACK: A Subroutine Package for Automatic Integration*, Series in Computational Mathematics, Vol. 1 (Springer Verlag, Berlin, 1983), 10.1007/978-3-642-61786-7.

[83] A. Deur, S. J. Brodsky, and G. F. de Teramond, The QCD running coupling, Nucl. Phys. **90**, 1 (2016).